Comparisons between Mesoscale Model Terrain Sensitivity Studies and Doppler Lidar Measurements of the Sea Breeze at Monterey Bay

LISA S. DARBY AND ROBERT M. BANTA

National Oceanic and Atmospheric Administration/Environmental Technology Laboratory, Boulder, Colorado

ROGER A. PIELKE SR.

Department of Atmospheric Science, Colorado State University, Fort Collins, Colorado

(Manuscript received 1 May 2001, in final form 27 April 2002)

ABSTRACT

A NOAA/Environmental Technology Laboratory Doppler lidar measured the life cycle of the land- and sea-breeze system at Monterey Bay, California, in 1987, during the Land–Sea Breeze Experiment (LASBEX). On days with offshore synoptic flow, the transition to onshore flow (the sea breeze) was a distinct process easily detected by lidar. Finescale lidar measurements showed the reversal from offshore to onshore flow near the coast, its gradual vertical and horizontal expansion, and a dual structure to the sea-breeze flow in its early formative stages. Initially, a shallow (<500 m) sea breeze formed that later became embedded in a weaker onshore flow that was ~1 km deep. Eventually these two flows blended together to form a mature sea breeze about 1 km deep.

Regional Atmospheric Modeling System (RAMS) two-dimensional simulations successfully simulated this dual structure of the sea-breeze flow when both the coastal mountain range just east of Monterey Bay and the Sierra Nevada range, peaking 300 km east of the shore, were included in the domain. Various sensitivity simulations were conducted to isolate the roles played by the land–water contrast, the coastal mountain range, and the Sierra Nevada range. Notable results included the following: 1) the Sierra Nevada range greatly affected the winds above 1500 m at the shore, even though the peak of the mountain range was 300 km east of the shore; 2) the winds at the shore, below 1500 m, were most affected by the land–sea contrast and the coastal mountain range; and 3) the presence of the coastal mountain range enhanced the depth of the sea-breeze flow but not necessarily its speed.

A factor separation method was employed to further isolate the contributions of the terrain and land–water contrast to the vertical structure of the modeled *u* component of the wind. When both mountains were included in the domain, the interaction of the slope flows generated by these mountains acted to strongly enhance onshore flow early in the morning. In contrast, the interaction of flows generated by the land–water contrast and the sloping terrain had its strongest effect late in the afternoon and early evening, working to oppose the sea-breeze flow. The triple interaction of the flows generated by the coastal mountain, inland mountain, and the land–water contrast enhanced the sea-breeze flow from the surface to 500 m above the sea level throughout the day.

1. Introduction

a. Motivation

The sea breeze is a thermally direct circulation that has been studied with varying degrees of sophistication for many years (Atkinson 1981; Pielke 1984; Simpson 1994). Spending time near the shoreline of any large body of water allows one to qualitatively experience the diurnal cycle of the breezes associated with the land–water temperature contrast. Its simplicity lends itself well to analytical and numerical modeling. However, many components of the sea breeze have been difficult for researchers to measure in detail, such as the vertical and horizontal structure of the winds over the water. Other complicating factors include the effects of inland topography; for example, inland mountain ranges generate their own thermally forced slope flows, which interact with the sea breeze. Along the coast of central California the diurnal flow behavior is driven by the land–sea contrast and two ranges of mountains. The following is a study of these interactions.

The development of clear-air remote sensing instrumentation has allowed researchers to observe the land- and sea-breeze cycle in detail. A Doppler lidar devel-

Corresponding author address: Lisa S. Darby, NOAA/ETL, R/E/ET2, 325 Broadway, Boulder, CO 80305.
E-mail: lisa.darby@noaa.gov

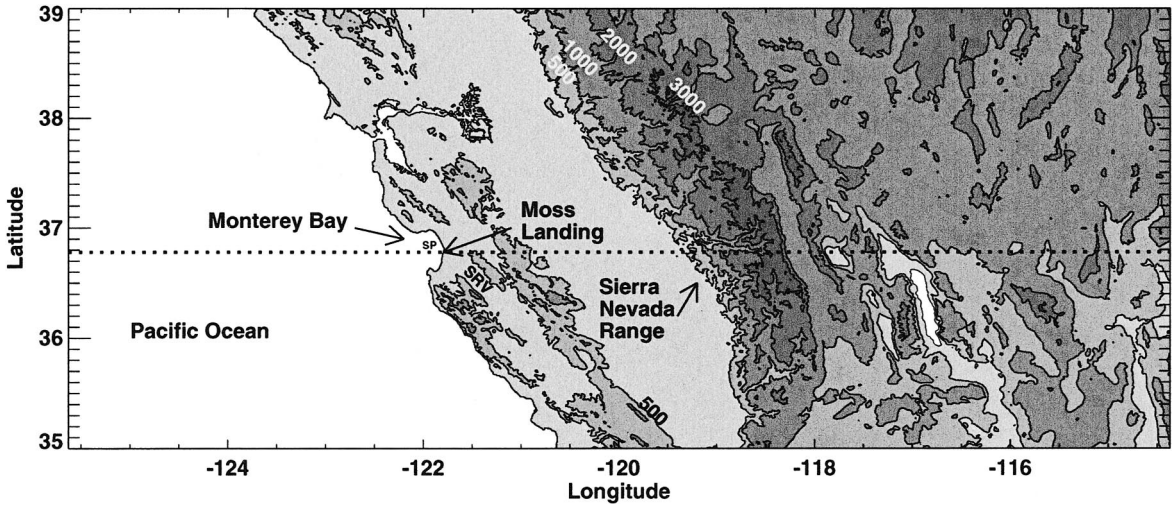

FIG. 1. Terrain map showing the location of LASBEX and the vast changes in topography across the modeling domain. The dotted horizontal line indicates the location of the 2D domain used in the simulations presented in this paper. It is the same latitude as the lidar deployment at Moss Landing, CA. Contours are every 1000 m except for a 500-m contour added for more detail between the Sierra Nevada range and the coast. The approximate location of the R/V *Silver Prince* is indicated by SP, the Salinas River valley by SRV.

oped and deployed by the National Oceanic and Atmospheric Administration/Environmental Technology Laboratory (NOAA/ETL) measured the land- and sea-breeze circulations at Monterey Bay in central California, during the Land–Sea Breeze Experiment (LASBEX) in September 1987. Banta et al. (1993), discuss several topics relevant to the sea breeze at Monterey Bay during LASBEX, including the topography surrounding Monterey Bay, the synoptic conditions encountered, the role of the subtropical high, and a classification scheme used to categorize the lidar data according to the transition to sea-breeze flow. It was shown that properties of the sea breeze that the lidar is well suited to measure include the initiation and the vertical and horizontal expansion of the sea-breeze layer, the horizontal variability and vertical structure of the winds, and the presence or absence of a return flow. Supporting measurements included winds and thermodynamic data from soundings.

Stationed at Moss Landing (Fig. 1) ~1.5 km from the shore, the ETL lidar regularly scanned from horizon to horizon along an east–west line (perpendicular to the shore), capturing the evolution of the land- and sea-breeze flows under different synoptic conditions. On three days during LASBEX that began with offshore synoptic flow, time series of Doppler lidar measurements perpendicular to the shore indicated that the vertical structure of sea-breeze winds included two scales of flow in the vertical and in time: a shallow, stronger sea breeze and a weaker, deeper sea breeze forming later in the day (Banta et al. 1993). These two flows eventually merged into a well-blended layer of onshore flow ~1 km deep.

A more extensive look at this aspect of the Doppler lidar measurements is presented in Banta (1995), where data from the three offshore flow days are analyzed. It is hypothesized that a local-scale temperature contrast at the shoreline drives the earlier, shallow sea breeze, whereas a larger-scale temperature contrast between the cooler ocean waters and the hot interior valley of central California drives the deeper sea breeze that develops later in the day. A coastal mountain range further enhances this temperature contrast by impeding the inland progress of cooler marine air. This dual-scale hypothesis has been put forth by other investigators who have observed the sea breeze along the west coast of the United States (e.g., Fosberg and Schroeder 1966; Johnson and O'Brien 1973).

The argument in these studies is essentially two-dimensional: that a long coastline with two parallel ranges of heated mountains will produce thermally forced onshore flow at two length (and depth) scales. The purpose of the present study is to use the Regional Atmospheric Modeling System (RAMS) to assess the validity of this argument, to see whether the model can reproduce these two vertical scales of onshore flow on a day with ambient offshore flow and, if so, to determine the roles of the various topographical features. We perform terrain sensitivity studies to give insight into the role that the complex terrain east of Monterey Bay plays in the vertical structure of the sea breeze. West–east cross sections from the two-dimensional model results will be compared to west–east cross sections of lidar data to determine how successful RAMS was at modeling the flow perpendicular to the shore at Moss Landing, and how certain terrain features affected the modeled flow. An alternative explanation for the two scales of flow is revealed in the model results: the land–water contrast is responsible for the shallow sea breeze, and the sudden onset of deep slope flow associated with the coastal

mountains is responsible for the weaker, deeper onshore flow. Of course, the 2D simulations and data analyses do not account for the 3D effects of the local terrain features.

The remainder of this section includes a brief discussion on how topography may influence the sea-breeze flow. Section 2 briefly reviews previous lidar observations of the sea breeze and gives an overview of the Land–Sea Breeze Experiment, with an emphasis on the Doppler lidar measurements. Previous modeling sensitivity studies and a description of the model setup used for the simulations presented in this paper are discussed in section 3. Section 4 contains model results from 2D simulations with various terrain configurations. Factor separation results are in section 5. A summary appears in section 6.

b. The role of topography in the development of the land- and sea-breeze circulation

Coastal topography is an important factor in the development of the sea-breeze circulation. Central California has coastal mountain ranges, a hot interior valley, and the steep Sierra Nevada range (Fig. 1). In describing the winds in the Central Valley of California, Frenzel (1962) summarized the main factors influencing the valley winds as: differential heating between land and water, diabatic heating of sloping terrain, and the constraining influence of topography. These factors can also be applied to the winds at Monterey Bay, as will be shown.

At the coast, gaps in nearby terrain through which the sea- and land-breeze flows can be channeled complicate the horizontal and vertical structure of sea and land breezes. Slope flows generated by nearby sloping terrain affect the time of onset and the depth of the onshore flow. These complications cause the structure of the sea breeze to deviate from theoretical predictions (Frenzel 1962).

The behavior of the sea breeze in the complex topography of Japan has lead researchers to conclude that inland mountain ranges (more than 100 km from the shore) also affect the sea-breeze flow (Kitada et al. 1998; Kimura and Kuwagata 1993). As for the United States, Pacific coast modeling studies that address the issue of inland topography include Lu and Turco (1994) and Cui et al. (1998).

2. Sea-breeze observations

a. Previous observations

The introduction of lidars to the research community has helped to alleviate some of the restrictions on the temporal and spatial scales of measurements experienced in earlier sea-breeze experiments. Measurements of the sea breeze using ground-based lidar include the work of Nakane and Sasano (1986), documenting the shape and turbulent structure of the sea-breeze front on the Kanto Plain of Japan (~60 km NE of Tokyo) using an aerosol lidar. Kolev et al. (1998) deployed a ground-based aerosol lidar on the shore of the Black Sea, paired with pilot balloon measurements, capturing the transition from offshore to onshore flow. Other studies used ground-based lidar to assess the influence of the sea breeze on the properties of aerosols in coastal regions, including that of Kolev et al. (2000), Murayama et al. (1999), and Vijayakumar et al. (1998). A differential absorption lidar measured vertical profiles of ozone in the Athens, Greece, area during a sea-breeze event (Clappier et al. 2000). While all of these studies contribute to the knowledge of the sea-breeze phenomenon, the NOAA/ETL measurements are the first from a ground-based Doppler lidar deployment to a sea coast to study the details of the land- and sea-breeze circulation. Carroll (1989) had earlier used data from an airborne Doppler lidar to study aspects of the California sea breeze.

b. The Land–Sea Breeze Experiment (LASBEX)

During LASBEX, wind measurements from a NOAA/ETL Doppler lidar deployed at Monterey Bay provided a new view of the vertical and horizontal structure of the winds over many hours at a time. Sweeps of lidar data take 3 min or less to complete, allowing for high temporal resolution surveillance of wind features and the transitions that occur in response to the diurnal heating and cooling cycle. Features measured by the lidar included the transitions between offshore and onshore flow, the vertical and horizontal expansion of the sea-breeze flow, the variability of the flow due to the nearby terrain, the absence of a Coriolis effect on the sea-breeze winds, and the absence of a consistent, compensatory return flow (Banta et al. 1993; Banta 1995). One of the most significant and interesting findings was the two scales of onshore flow, seen in the time–height series of the lidar measurements of the u component of the wind, as a shallow sea breeze that becomes embedded in a weaker, deeper sea breeze on days with ambient offshore flow. The details of LASBEX, including information on other instruments deployed, can be found in Intrieri et al. (1990).

1) DOPPLER LIDAR

The technical aspects of the Doppler lidar deployed at LASBEX are discussed in Post and Cupp (1990). Two general characteristics of lidar that set it apart from radar are a narrow beam and no ground clutter. The narrow beam allows for high-resolution measurements (radial velocity and backscatter are measured simultaneously), and the lack of ground clutter allows the lidar to obtain these measurements close to terrain. These characteristics make the lidar particularly useful for measuring wind flow in complex terrain settings (e.g., Banta et al. 1997, 1999; Darby et al. 1999).

The lidar scanning strategy included vertical-slice (constant azimuth while varying in elevation) and conical (constant elevation angle while varying in azimuth) scans. The east–west vertical cross sections proved invaluable for assessing the vertical structure of the land- and sea-breeze flows. Measurements from these scans are central to this study. Low-elevation-angle (1°–3°) conical scans revealed much information about the horizontal variability of the winds at Monterey Bay.

2) DATA ANALYSIS

As presented in Banta et al. (1993) and Banta (1995), a day with a distinct transition from offshore to onshore flow, 16 September 1987, was chosen for extensive analysis. The lidar operated from early morning into the night, capturing the transition from early morning offshore flow to onshore flow, the maturation of the sea breeze during the day, and the reversal back to offshore flow in the evening. The synoptic setting for 16 September 1987 is described in Banta et al. (1993). Because of a synoptic-scale cold front passage through Washington State on 15 September 1987, a high pressure center over central Idaho, and the subsequent passage of the cold front past Monterey Bay, the large-scale low-level flow was offshore rather than onshore. Consequently, the subtropical high was not the dominating synoptic-scale factor at Monterey Bay on 16 September. This is a deviation from the normal summertime regime for the west coast of the United States. When the subtropical high dominates, the temperature contrast between land and water is enhanced due to cold water upwelling near the coast, and the prevailing winds are from the northwest.

Lidar radial velocity plots for conical scans at 1° elevation are shown in Fig. 2. Negative velocities (green and blue) indicate flow toward the lidar, and positive velocities (orange and red) indicate flow away from the lidar, positioned at the center of each plot. The early sea breeze is very shallow, so it is important to note that the height of the lidar beam, relative to the lidar, increases with distance from the lidar. Even when the elevation angle is 1° or 2°, changes with distance along the beam could be because of horizontal variability, or could be a result of the beam penetrating through very shallow layers.

In Fig. 2a, taken at 0829 local standard time (LST = UTC − 8 h), 16 September 1987, at a 1° elevation angle, the offshore flow nearer the surface (measurements closest to the lidar) was from the southeast. These winds were oriented along the direction of the Salinas River valley (SRV in Fig. 1). Above this southeasterly flow (measurements farther away from the lidar), the flow was from the northeast. Higher elevation scans (not shown) indicated northwesterly flow above that. Figure 2b shows a small region of onshore flow west of the lidar, the newly formed sea breeze. The offshore flow from the Salinas River valley had weakened considerably and the sea breeze was starting to flow into the valley. In addition to this flow toward the southeast, the horizontal extent of the sea-breeze flow was enhanced east of the lidar (the elongated region of westerly flow at ~90° azimuth), probably due to upslope flow generated by the nearby terrain. In Figs. 2c and 2d the sea breeze continued to strengthen and expand. A gap in the terrain to the northeast of the lidar continued to channel the larger-scale offshore flow while the onshore flow was in its developmental stage. Figure 2e shows stronger onshore flow at lower heights over water, with light and variable winds above (farther in range from lidar), whereas the winds over the land were more uniform with distance, which suggests that they were also more uniform with height. A mature sea breeze is shown in Fig. 2f. Note that the strongest flow over land in the bottom two plots was oriented along the Salinas River valley. These examples of lidar measurements show the complexity of the winds in the Monterey Bay region. Both the land–water contrast and the surrounding terrain play significant roles in the horizontal variability of the wind.

Figure 3 shows a similar series of conical lidar scans, but with an elevation angle of 5° above the horizon, thus providing more information about the winds higher above the ground than the 1° plots. At 0726 LST (Fig. 3a) the directional shift of the flow with height was very clear with southeasterly flow from the Salinas River valley near the surface and east-northeasterly flow above that. The newly formed sea breeze was seen as a very weak westerly to northwesterly wind near the surface in Fig. 3b. Figure 3c shows the two scales of sea-breeze flow, stronger onshore flow at low levels, and weaker onshore flow above, as described in the introduction. The strengthening of the sea breeze over a half hour's time is seen in the comparison of Fig. 3c and Fig. 3d. By 1709 LST (Fig. 3e), the two scales of flow had blended, and the wind near the surface was now south-southwesterly. A few hours later, in the evening (Fig. 3f), the flow at the surface still had a southerly component, but the flow above this layer had switched to offshore.

Figure 4 displays six panels of constant-azimuth vertical-slice scans showing the evolution of the vertical structure of the sea breeze along a line perpendicular to the coast on 16 September 1987. Again, negative (blue/green) velocities indicate flow toward, and red and orange indicate flow away from, the lidar. In Fig. 4a, the early morning offshore flow was ~1.5 km deep, with a very shallow layer of onshore flow at the surface. This precursor to the sea breeze, which is discussed in Banta et al. (1993), was determined to be a short-lived, disorganized flow resulting from turbulent processes. The flow above the offshore layer had a westerly component. Almost 2 h later, at 0949 LST, a very shallow (<100 m) sea breeze had formed underneath the morning offshore flow (Fig. 4b). The landward extent of the onshore flow was much greater than the seaward extent, as seen

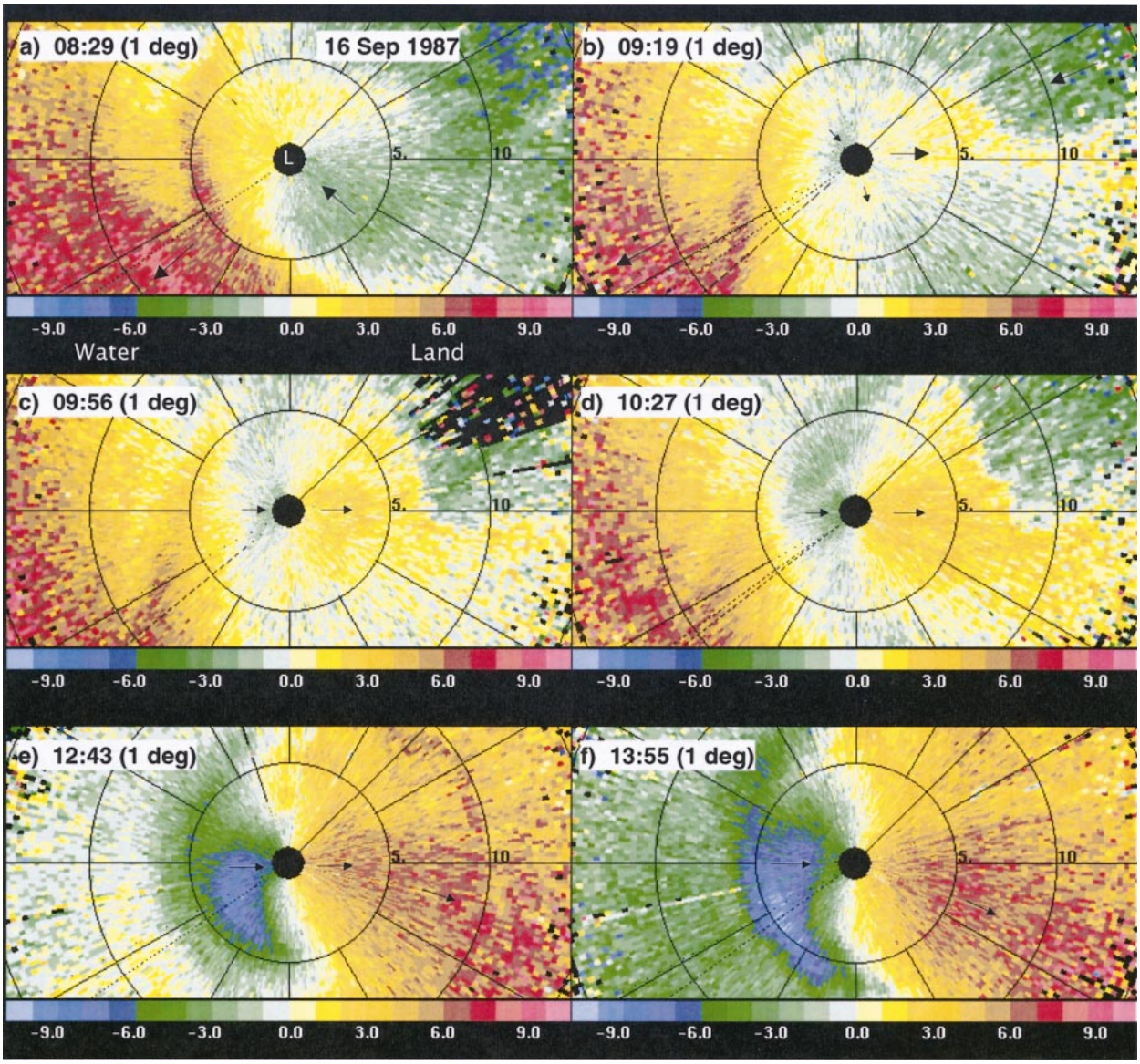

FIG. 2. Doppler lidar constant-elevation-angle radial velocity scans showing the evolution of flow near the shore on 16 Sep 1987. The lidar (indicated by an L in the top-left scan) is in the center of each scan and was located 1.5 km east of the shore. The lidar's minimum range was 1.5 km, so measurements on the left-hand side of each plot are over water, whereas measurements on the right-hand side are over land. Green and blue indicate flow toward the lidar; orange and red indicate flow away from the lidar. Range rings are 5 km apart. Wind speeds are in m s^{-1} (the white numbers under the color scale). Times are LST. Elevation angle is 1° above the horizon. Flows are described in text. Black arrows (in this and subsequent lidar figures) serve merely as reminders as to whether the winds were flowing onshore or offshore.

in the constant-elevation angle scans in Fig. 2. The two scales of sea breeze were evident at 1226 LST (Fig. 4c). A shallow (<250 m deep) layer of onshore flow was several meters per second stronger than the weaker onshore flow developing between 250 and ~1000 m. The sea breeze was deeper over land than over water, and the winds were stronger over the water surface, indicating an asymmetry in the sea-breeze development. The stronger winds are probably due to less surface roughness over the water than over the land, and a deeper boundary layer over the warmer land surface would allow a deeper layer of onshore flow to form. Traces of the early morning offshore flow existed above the sea breeze.

Over water, the sea-breeze flow deepened as it approached the shore, and the winds over the water's surface continued to be stronger than the winds over land (Fig. 4d). The onshore flow was now at least 6 m s^{-1} from the surface to 500 m above ground level (AGL) over land. A mature sea breeze 1 km deep was observed

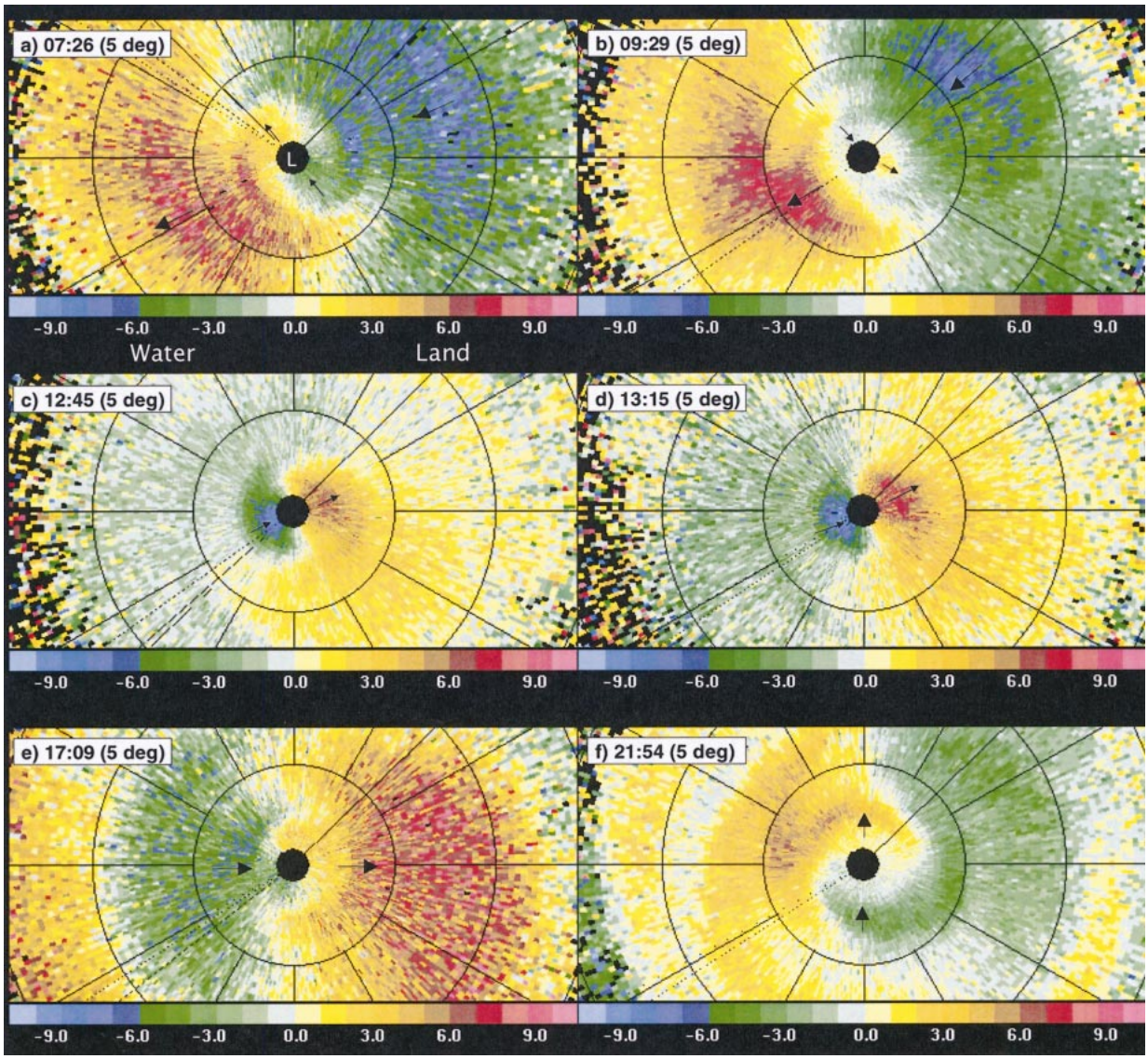

FIG. 3. As in Fig. 2 except that the elevation angle was 5° above the horizon.

at 1712 LST (Fig. 4e) with a layer of offshore flow above it, also ~1 km deep. The westerly component of the synoptic-scale, upper-level northwesterly flow was seen above that (as in the previous plots). Offshore flow was reestablished in the evening, by 2200 LST, as shown in the final panel of Fig. 4f, taken several hours after the scan shown in Fig. 4e. The complexity of the winds shown in the constant-elevation scans (Figs. 2 and 3) clearly demonstrates that these vertical east–west scans cannot possibly tell the whole story of the sea-breeze flow, but they are a very good starting place for investigating the vertical structure of the sea breeze at Monterey Bay.

Radial velocity data from all east–west vertical-slice scans taken on 16 September 1987 were transformed from polar coordinates to Cartesian coordinates. A horizontal average of the u component of the wind from $x = -4$ to -1.5 (i.e., just offshore) was calculated at the height of each vertical grid point (vertical grid spacing was 25 m). Thirty-one of these profiles from vertical-slice scans taken on 16 September were compiled into the time–height plot shown in Fig. 5. Similar time–height plots created from the sea breezes modeled with RAMS will be shown in section 4. The comparisons between this lidar plot and the model time–height plots will be used to assess the model's success in capturing the vertical structure of the Monterey Bay sea breeze; therefore, it is important to review here the features of interest in the lidar plot.

In the morning hours (0700–1000 LST) the offshore flow was at least 1.5 km deep, as seen in the color plots (Fig. 4), with a maximum speed of 7 m s^{-1} just before

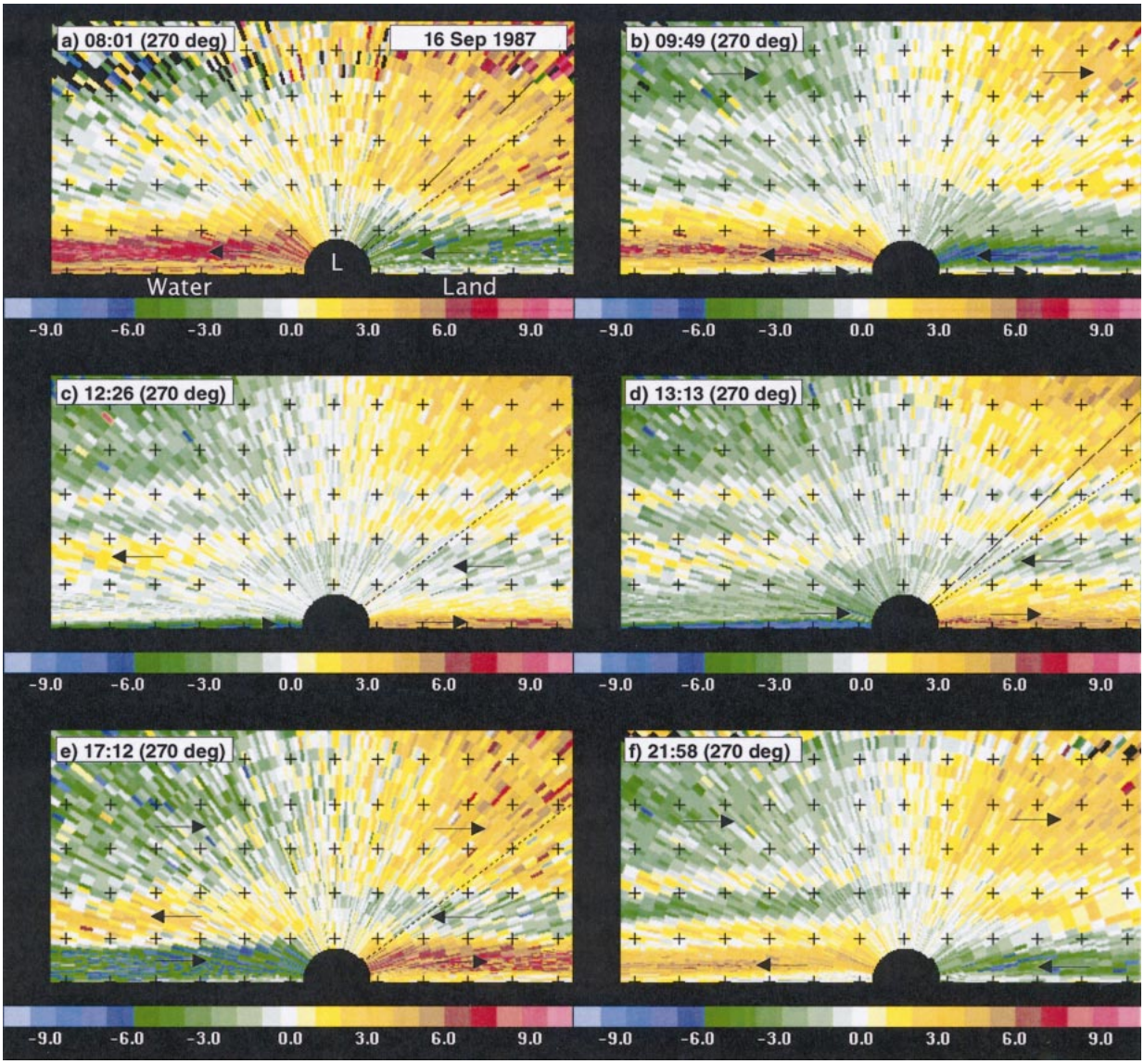

FIG. 4. Doppler lidar east–west constant-azimuth-angle radial velocity scans for 16 Sep 1987. The location of the lidar is indicated by an L in the top left-hand plot. As in the constant-elevation-angle plots, measurements to the left of the lidar are over water, measurements to the right of the lidar are over land. Green and blue indicate flow toward the lidar; orange and red indicate flow away from the lidar. The vertical axis is height above the lidar, and the horizontal axis is distance from the lidar (tick marks 1 km apart). Flows are described in the text.

0800 LST. Above this offshore flow was a layer of weak westerly flow. The reversal from offshore to onshore flow was first indicated at the surface at 0930 LST. The onshore flow layer was quite shallow (<250 m) for the first hour, then rapidly increased in depth at 1200 LST. The shallow, stronger sea breeze and the weaker, deeper sea breeze were evident until 1500 LST. Finally, the mature, blended sea-breeze stage was evident for more than 4 h starting at ~1500 LST. The apparent weakening of the wind below 500 m between 1800 and 2000 LST was actually a gradual backing of the wind from westerly to southerly, as seen in the conical-scan color plots, so the radial component of the wind became small in the east–west cross sections. After 2200 LST, the reversal from onshore to offshore flow began at the surface.

3. Mesoscale model sensitivity studies investigating the land–water contrast and terrain effects

Numerous features of the sea-breeze circulation are of interest to researchers, especially the vertical structure of the sea-breeze winds, vertical temperature profiles associated with the sea breeze, and the sea-breeze front. These features are important for air pollution transport and dispersion issues, a common motivation

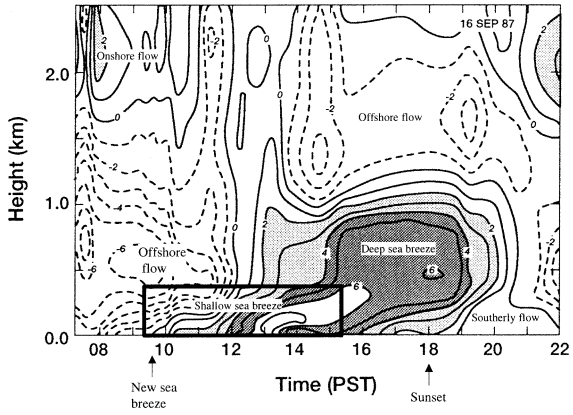

FIG. 5. Time–height series of vertical profiles of the *u* component of the wind as measured by the ETL Doppler lidar (from Banta et al. 1993). Dashed lines represent flow from the east (offshore); solid lines, flow from the west (onshore). Westerly flow 2–4 m s^{-1} has light shading, flow from 4 to 6 m s^{-1} has heavier shading. Height is km AGL (the lidar was 15 m above sea level (ASL).

for studying the sea breeze (e.g., Eastman et al. 1995; Kitada et al. 1998; Kotroni et al. 1999; Lyons and Olsson 1973; Lu and Turco 1994). Measurement programs of sea-breeze phenomena are usually limited in the areal distances they can cover, and accordingly they are limited in the number of features they can measure, especially features of different length scales. It is difficult to simultaneously measure the sea breeze with high spatial and temporal resolutions. If the focus is on the vertical structure, as it often is, then the horizontal variability of the winds will be missed. If the terrain is complex in a coastal region, the characteristics of the sea breeze are even more difficult to isolate. Because of these difficulties, investigators have turned to numerical modeling to better understand the sea breeze.

Conducting sensitivity studies based on numerical modeling results has been a long-standing practice in assessing the dynamical processes associated with various mesoscale phenomena. With the development of the early sea-breeze models came sensitivity experiments, beginning with Estoque (1962), who investigated the direction of the synoptic wind relative to the shore and its effect on the sea breeze. Other sensitivity studies include McKendry (1992), Pielke (1974), Xu et al. (1996), Doyle (1997), and Arritt (1987). Mahrer and Pielke (1977) were the first to present model comparisons of sea breeze, slope flows, and the combination of both.

The RAMS, based in part on Pielke's (1974) sea-breeze model, has evolved into a sophisticated atmospheric model that can handle a wide range of meteorological scales. All of the RAMS simulations shown in this paper are two-dimensional (2D). According to Avissar et al. (1990), the needed domain size and grid spacing for mesoscale numerical modeling of sea and land breezes with homogeneous initialization are at least

TABLE 1. Simulation number with corresponding terrain configuration.

Simulation	Terrain
With land–water contrast	
1	Smoothed terrain
2	Inland mountain and coastal mountain
3	Coastal mountain
4	Inland mountain
5	Flat terrain
Without land–water contrast	
6	Smoothed terrain
7	Inland mountain and coastal mountain
8	Coastal mountain
9	Inland mountain
10	Flat terrain

1000 and 20 km (or smaller), respectively. In our case, the east–west domain size was 1000 km, large enough to extend from well west of the bay to the east of the Sierras, and falling within the limits of what Avissar et al. (1990) suggested. The dotted line in Fig. 1 represents the domain, an east–west cross section through the center of Monterey Bay at the same latitude as the lidar deployment at Moss Landing. The western third of the domain extended over Monterey Bay and the Pacific Ocean. A constant sea surface temperature of 15°C, determined from the monthly average for September 1987, was assigned to the water portion of the domain. The upper boundary condition was a rigid lid with an ab-

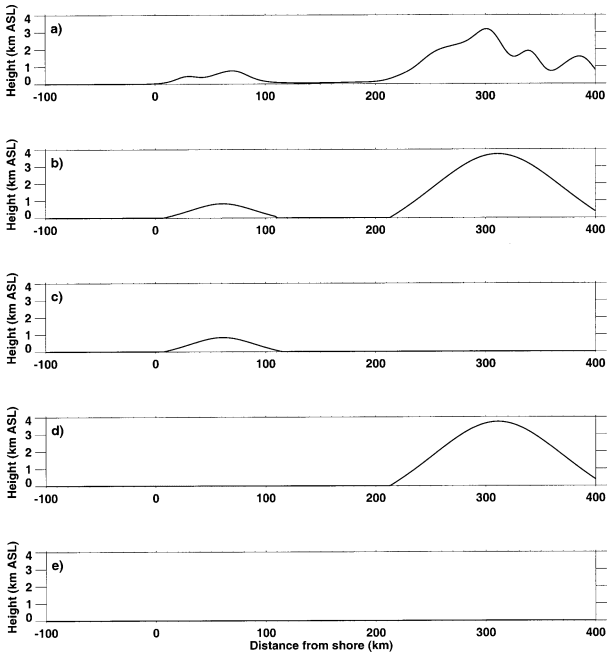

FIG. 6. The terrain profiles used in the model sensitivity studies. Only the part of the domain immediately surrounding the terrain is shown: (a) smoothed realistic terrain, (b) idealized dual mountain, (c) idealized coastal mountain, (d) idealized inland mountain, and (e) flat terrain.

sorbing layer, and the lateral boundary conditions were based on Klemp and Wilhelmson's (1978a,b) work. The surface layer flux parameterization was based on the Louis (1979) scheme. The land surface parameterization used the soil model described in Tremback and Kessler (1985) and a vegetation scheme based on Avissar and Pielke (1989). The vegetation class was arbitrarily specified to be short grass for all land grid points.

The simulations were designed to have high vertical resolution because the focus of this study is the vertical structure of the sea breeze. The vertical grid spacing from the surface to 1.0 km AGL was 25 m. Above 1.0 km AGL, the grid spacing increased gradually with height, never exceeding 500 m. A total of 90 grid points in the vertical featured one-half the grid points in the lowest 1.2 km AGL. The domain height was 15 km. Because of the steep slope of the Sierra Nevada range to the east of Monterey Bay, and the desire for high vertical resolution, it was necessary to have a relatively small horizontal grid spacing, $\Delta x = 2$ km, for the single-grid domain.

A modified morning sounding launched from the R/V *Silver Prince* (located 11 km offshore, approximate location indicated by SP in Fig. 1) on 16 September 1987 was used for the homogeneous initialization. A strong marine inversion was represented in the sounding, as is typical of the region. Since this profile only extended to 7 km AGL, the 16 September 1987 morning rawinsonde from Oakland, California, was used to fill out the sounding to the top of the domain. Winds below 5 km ASL in the initial sounding were easterly at 1 m s^{-1}, backing to westerly by 6.5 km ASL. The simulations, which began at 1200 UTC (0400 LST) 15 September, were run for 42 h to allow the model to complete one diurnal cycle before being analyzed, as recommended by Avissar et al. (1990) and Cui et al. (1998) when the domain is large and homogeneous initialization is used.

The Coriolis parameter was turned off in the model simulations, yielding true two-dimensional simulations. In a 2D complex terrain simulation, the wind flow is not able to adjust realistically after it is perturbed from geostrophy. The mountains in our simulations produce a very large perturbation. When the Coriolis parameter was activated, the model became unstable in the afternoon when the sea breeze became established and the winds became supergeostrophic, resulting in an acceleration of the winds out of the model domain (i.e., to the north or south). In the real world, pressure gradients would develop in response to this perturbation in the north–south direction, preventing the flow from accelerating unrealistically. No such freedom to adjust is present in a 2D model.

Table 1 shows the various simulation experiments used for the sensitivity studies of topography and land–water contrast. The first group of simulations, 1–5, comprises the terrain sensitivity set with a land–water contrast included in the domain. The only change in the model input among these simulations was the shape of the terrain. Figure 6 schematically shows the different terrain configurations. In simulation 1 the terrain was read from a 30″ terrain dataset, interpolated to the model grid and smoothed (Fig. 6a). A more idealized version of the terrain was implemented in simulations 2–4 (Figs. 6b–d) and will be referred to as the idealized terrain. The coastal mountain represented the rising terrain directly east of Monterey Bay (see map, Fig. 1) and the inland mountain, peaking 310 km east of the shore, represented the Sierra Nevada range. Simulation 2 had both mountains, simulation 3 included only the coastal mountain, and simulation 4 included only the inland mountain. Simulation 5 had only flat terrain (Fig. 6e). In this group of simulations the western 325 km of the domain was water and the remaining portion of the domain was land.

In the second group of simulations, 6–10, the entire domain consisted of land grid points (i.e., no water in the domain) with a vegetation classification of short grass. The same five terrain variations used in the first group were also used here. The water was eliminated to isolate the effects of the slope flows from the sea-breeze flow. Results from the flat terrain cases will not be shown.

4. Model results

a. West–east cross sections

Figures 7–10 show west–east (left–right) cross sections of contours of the *u* component of the wind for simulations 1–4. Only the region of most interest has been plotted; the domain extended another 300 km east and 250 km west of the region shown and the domain height was 15 km. The west–east cross sections show the vast differences in the vertical structure of the sea breeze and slope flows when the terrain was varied.

The simulation with smoothed terrain is shown in Fig. 7. In the earliest plot shown, 0800 LST (Fig. 7a), both mountains had a shallow layer of downslope flow, most easily identified as the thin layer of dashed contours attached to the western slopes of both mountain ranges. The noise in the contours west of the steep terrain of the inland mountain, 2–3 km above sea level (ASL), disappeared as the land surface heated during the day. The combination of a stable layer at the surface that suppressed vertical mixing, steep terrain, and high vertical resolution was responsible for the noise. Since the noise is occurring under stable conditions (nighttime and early morning) the model may be attempting to force the formation of gravity waves with wavelengths at or near the resolution of the model. There may also be truncation errors in the pressure gradient force calculations in regions of steep topography.

The shore is near $x = 0$ km, so when the contours switch to positive (solid) in this region, this is an in-

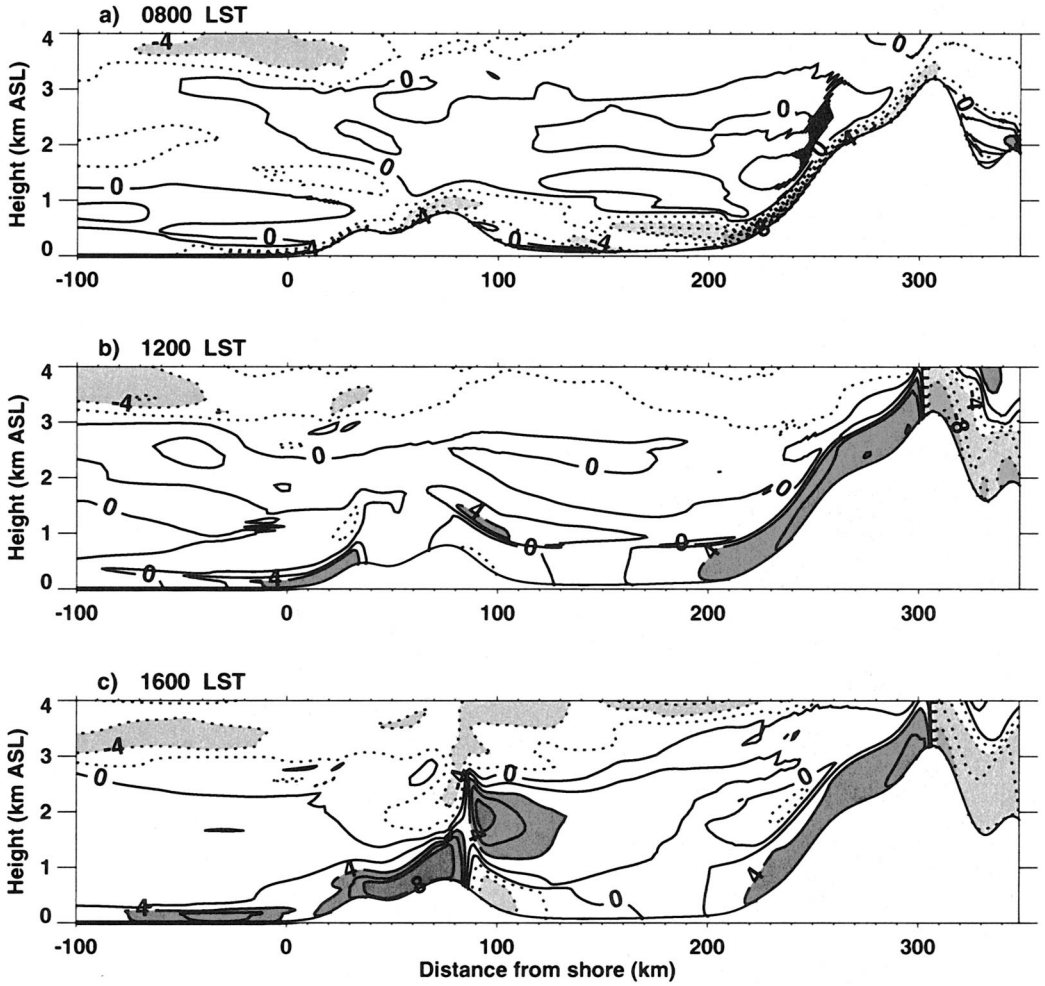

FIG. 7. West–east cross sections of the modeled u component of the wind (in m s^{-1}). Plots are every 4 h from 0800 to 1600 LST for the smoothed terrain case. Solid (positive) contours indicate westerly flow, and increment every 2 m s^{-1}. Speeds greater than 4 m s^{-1} are shaded with darker gray shades. Dashed (negative) contours indicate easterly flow, also incrementing every 2 m s^{-1}. Speeds with magnitude greater than 4 m s^{-1} are shaded with lighter gray shades. The shore lies at $x = 0$ km, with water filling the domain west (left) of the shore. The terrain is very lightly shaded.

dication that the combined sea breeze–upslope flow is in progress. By 1200 LST (Fig. 7b) the sea breeze and upslope flows had started, now identified as the shallow dark gray layer on the western slopes, and the light gray layer or dashed lines on the eastern slopes. Over the course of the day, the upslope flow–sea breeze grew in both the horizontal and vertical dimensions. At 1600 LST (Fig. 7c) a well-defined solenoidal flow structure had developed for each mountain range: upslope flow on both sides of each mountain with a compensating return flow above. However, the return flow for the westward slope of each mountain range was quite weak. The convergence zone associated with the sea breeze crossed the crest of the coastal mountain by 1600 LST (Fig. 7c).

In the idealized-terrain simulation with both mountain ranges (Fig. 8) the terrain was slightly steeper than in the smoothed terrain case, so the fluctuations were stronger, giving the appearance of more noise along the slope of the inland mountain range in the early morning. Also, because of the steeper slopes, the downslope winds were stronger in this simulation relative to the smoothed terrain case. Overall, the vertical structure of the sea breeze was similar to the previous case shown, making this terrain setup suitable for sensitivity studies, such as comparing the differences in the winds at the shore with the coastal mountain only and inland mountain only cases.

With only the coastal mountain in the domain (Fig. 9), the main wind feature of the morning was a very shallow slope flow that was much more well defined and stronger on the landward side of the mountain. In fact, this downslope flow on each slope of the coastal mountain propagated away from the mountain with a

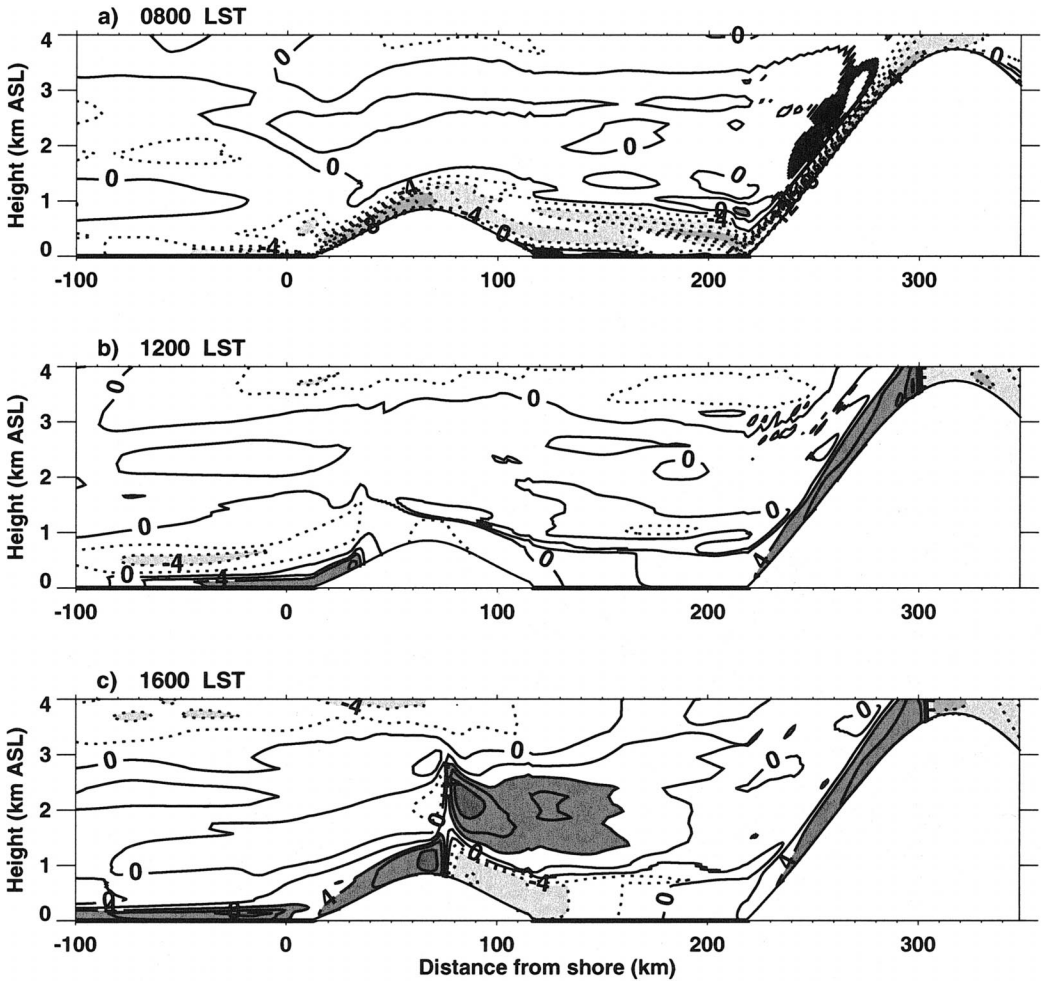

FIG. 8. As in Fig. 7 except for the idealized dual-mountain case.

density-current-like structure (0800 LST; Fig. 9a). As the temperature of the land increased, the upslope flows and their return flows became established. The solenoidal flow had a greater horizontal extent on the westward side of the mountain than on the eastern side, because of the addition of the sea-breeze flow. This particular asymmetry in the solenoidal flow is absent in the no-water case (shown later in Fig. 17b). The vertical structure of the flow was simpler in this case than in any other simulation that included sloping terrain.

Figure 10 shows the no-coastal-mountain case, with the inland mountain as the only mountain in the simulation. Strong downslope flow that developed during the night and its strong return flow dominated the winds in the morning. Whereas the downslope flow weakened considerably between 0800 and 1200 LST (Figs. 10a and 10b, respectively), the westerly flow above weakened very little, continuing to dominate the winds from 1 to 2.5 km ASL throughout the day. A shallow sea breeze is seen at 1600 LST (Fig. 10c).

The results for the case with flat terrain (not shown) indicated that the strongest sea-breeze flow in any of the simulations, with a speed of 8 m s^{-1}, developed in a shallow layer, with a weak return flow above it. Ookouchi et al. (1978) also produced a stronger modeled sea breeze in their flat terrain case than in their mountain cases. These model results are consistent with observations; that is, the sea breezes at Melville and Bathurst Islands (Skinner and Tapper 1994), which have a maximum terrain height of approximately 120 m, are stronger than the sea breeze measured on Taiwan, which has a maximum terrain height of ~3000 m (Johnson and Bresch 1991; Chen and Li 1995). In the absence of terrain, the vertical structure of the sea breeze seemed to be constrained by the thermal structure of the air mass; that is, the onshore flow was confined to the inversion layer (not shown).

Figure 11 shows results from simulation 6, a simulation that had the same terrain configuration as simulation 1, but no water in the domain, only short grass. The winds at 0800 LST (Fig. 11a) were similar to the winds in the corresponding case with water (Fig. 7a), except for a greater westward extension of the slope flow on the west side of the coastal mountain in the

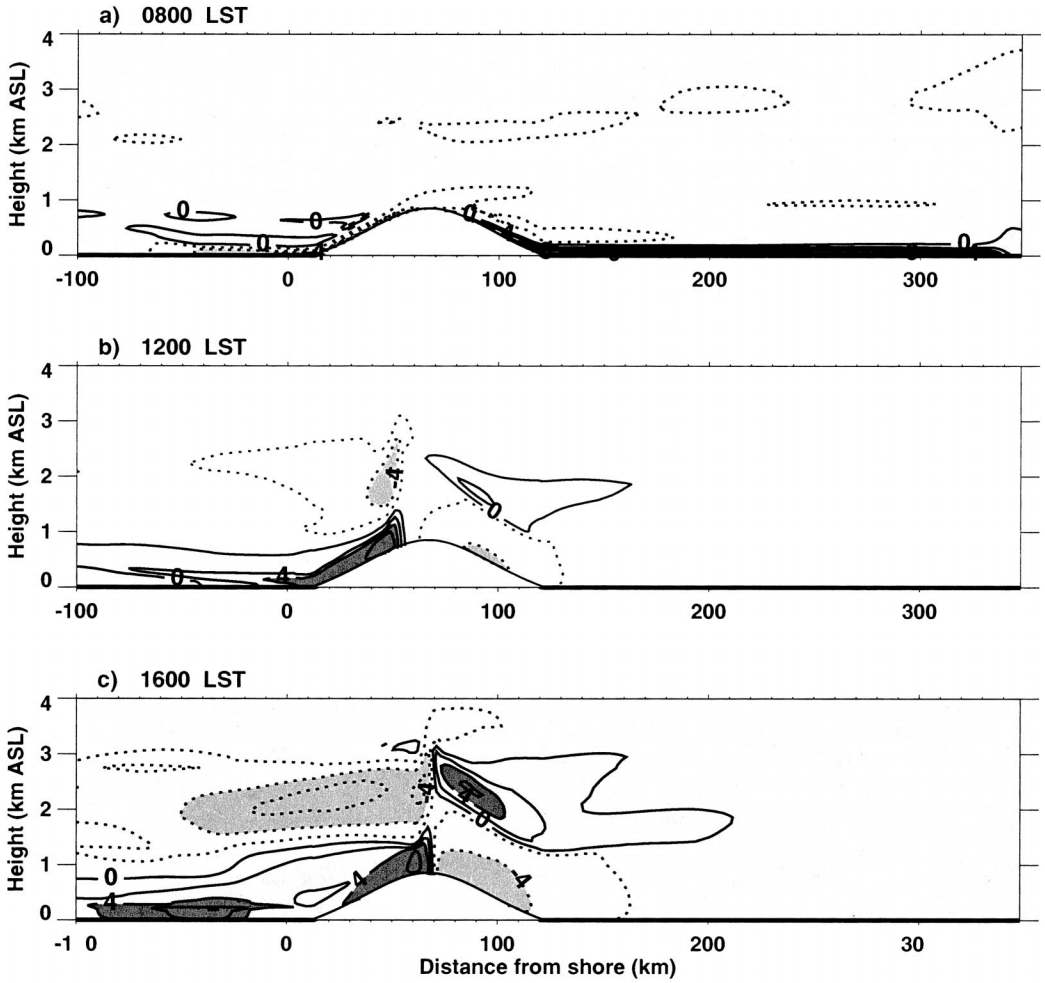

FIG. 9. As in Fig. 7 except for the idealized coastal-mountain case.

simulation without water. By 1200 LST (Fig. 11b), however, the winds were very different from the land–water contrast case west of the crest of the coastal mountain below 1 km ASL, yet almost identical east of the crest. Instead of the blended sea breeze and upslope flow, only a small region of weak upslope flow developed on the western side of the coastal mountain. With time (Fig. 11c), a deep upslope flow formed, but the winds were weaker than the winds in the combined sea breeze/slope flow in the corresponding case with water (Fig. 7). The upslope flow started later in the day without the enhancement from the land–water contrast. The solenoidal flow about the coastal mountain was more symmetrical than in the water case, as expected, but it was perturbed by the presence of the inland mountain. These characteristics were also seen in the other simulations that included the coastal mountain, but no water in the domain. The west–east cross sections for the remaining simulations without water will not be shown here, but some will be seen in the factor separation section (section 5). The results from all simulations with sloping terrain will be presented in the next section in time–height plots.

b. Time–height series

1) TERRAIN SENSITIVITY WITH THE LAND–WATER CONTRAST INCLUDED

To compare the model results with the lidar data, time–height series of the *u* component of the wind, compiled from profiles extracted from the shoreline grid point every 0.5 h of the simulation, were plotted in the same manner as the lidar time–height series shown in Fig. 5. Our intention is to compare the modeled time–height series with the Doppler lidar time–height series to assess the accuracy of the model results, and to attribute aspects of the lidar analysis to physical processes.

Model output time–height series of the *u* component of the wind for simulations including water in the western portion of the domain are shown in Fig. 12. The time–height series that most resembled lidar data (Fig.

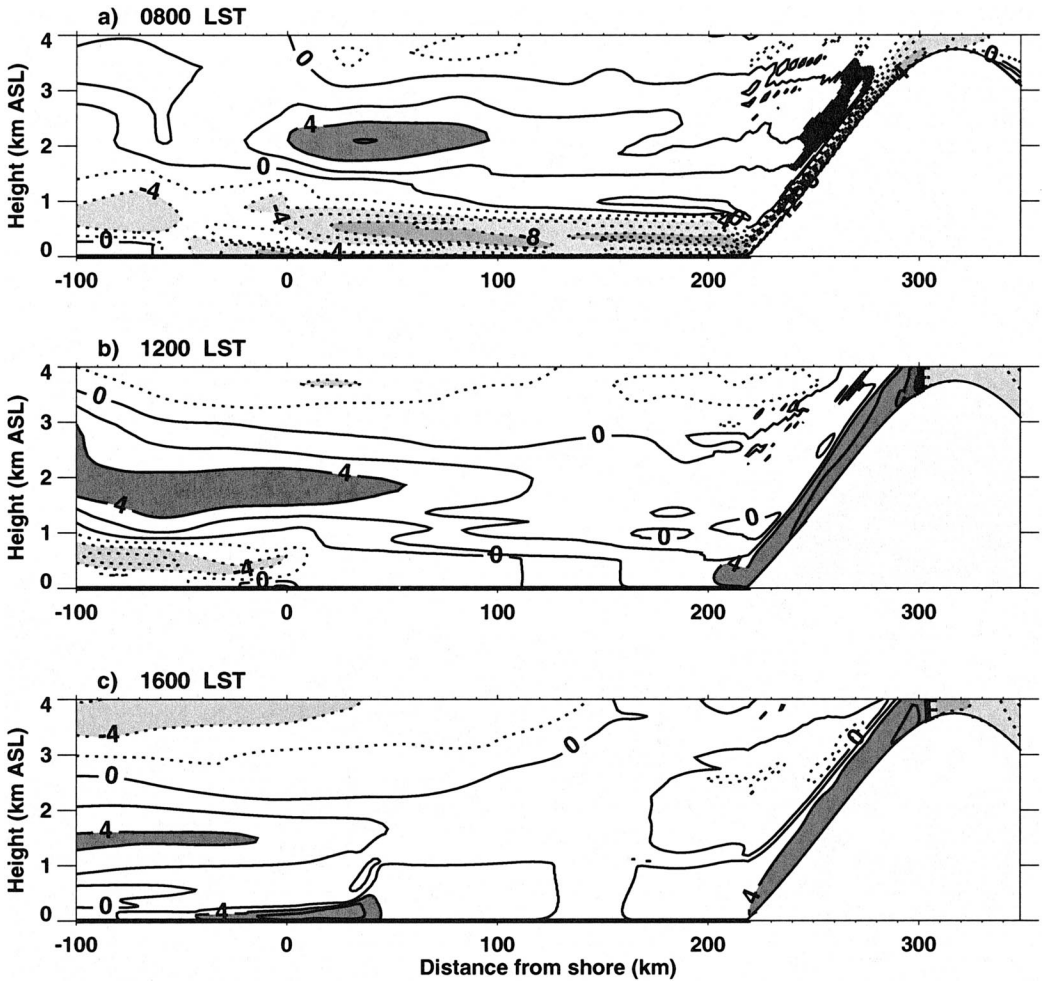

FIG. 10. As in Fig. 7 except for the idealized inland mountain case.

5) were the smoothed terrain and idealized dual-mountain simulations, Figs. 12a and 12b, respectively. Except for the absence of weak westerly flow in the morning above 2 km ASL, results shown in Fig. 12c (the coastal mountain only case) also closely resembled the lidar measurements.

Although the modeled sea breeze from simulation 1 was slightly weaker than the lidar-measured sea breeze, the overall structure of the sea breeze (solid contours) in this simulation was quite similar to lidar data (Fig. 5), including the two scales (shallow and deep) of onshore flow. Above 1500 m ASL there were some general similarities with measurements, such as short-lived weak westerly flow above 2 km early in the period shown, but the model results were more realistic in the lowest part of the domain, below 1.5 km AGL. While the lidar-measured and modeled sea breezes were similar, the structure of the early morning offshore flow was quite different. Even though it was almost as strong as in the lidar measurements, the modeled offshore flow was much shallower (Fig. 12a). This simulation was rerun with an initial sounding having a weaker inversion to see if the early morning offshore flow would be deeper. The strong offshore flow in the modified model results (not shown) was still much shallower than the lidar observations.

Notable similarities between Fig. 12b (idealized dual-mountain case) and lidar data (Fig. 5) include 1) a deep pre-sea-breeze offshore flow with speeds up to 6 m s^{-1} at ~300 m ASL; 2) shallow, stronger onshore flow beneath a weaker, deeper onshore flow; 3) the transition back to offshore flow below 1000 m ASL after sunset; and 4) the existence of onshore flow above 1500 m ASL early in the period shown. The most critical result of this simulation and the one shown in Fig. 12a is similarity 2 above, the appearance of the two scales of onshore flow. Indeed, the independence of the two scales of onshore flow seems more evident in these plots than in the measurements. The shallow sea breeze (flow below 300 m) was 2 m s^{-1} weaker than lidar measurements, but the maximum wind occurred at ~1300 LST, as in lidar measurements and surface station measurements (not shown). Although similarities were evident between lidar and RAMS results in the morning offshore flow, the vertical structure of this flow in the model results was more

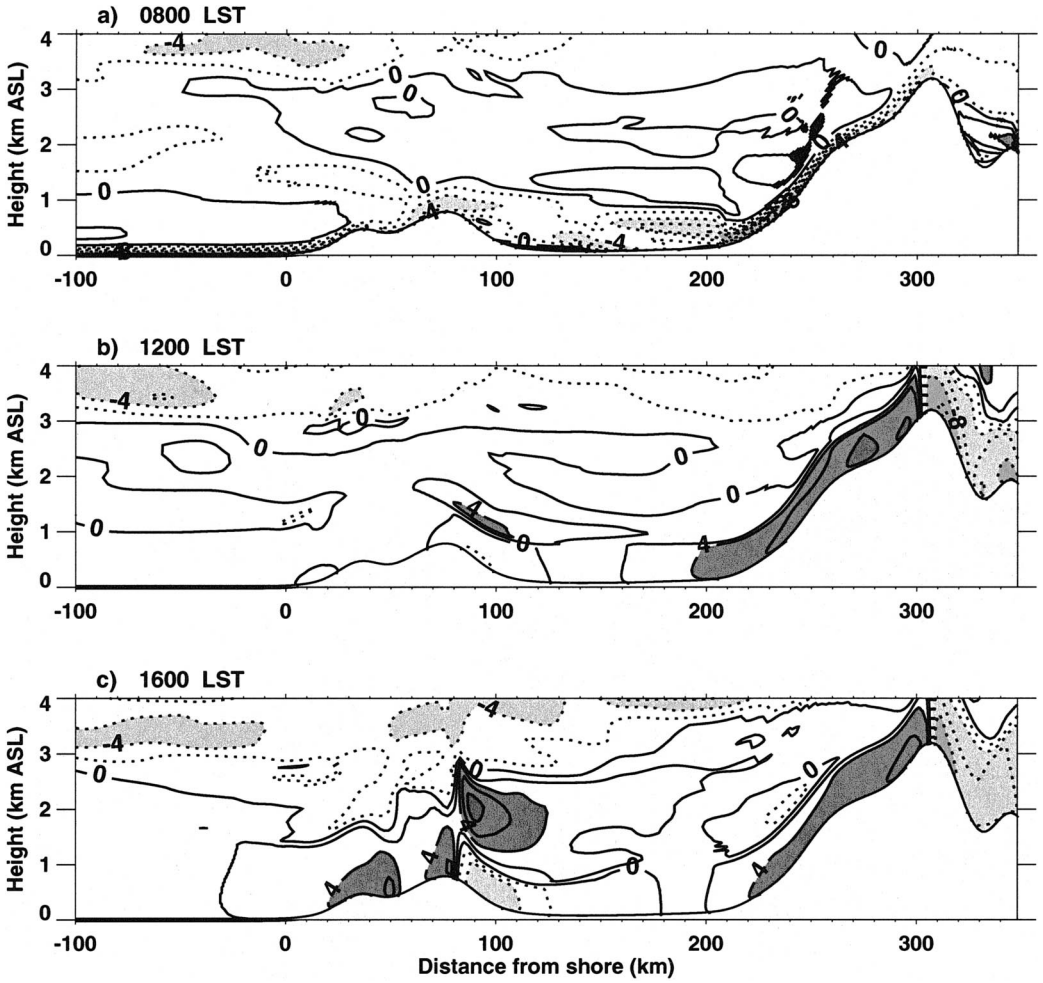

FIG. 11. As in Fig. 7 except there is short grass rather than water to the west (left) of $x = 0$ km.

''compressed'' than observed; that is, overall it was not as deep and the stronger speeds occupied a thinner layer, but it was closer to the lidar results than the smoothed terrain simulation. Again, the strongest similarities between model results and lidar data occurred in the lowest 1500 m of the domain. The offshore flow above the mature sea breeze in the lidar data does not appear in either of these simulation results (Figs. 12a or 12b).

The effects of removing the inland mountain are seen in the model results presented in Fig. 12c. In this simulation, only the coastal mountain was present. The structure of the sea-breeze flow itself was similar to the other simulations examined so far and to the lidar data, with a shallow, stronger layer of onshore flow beneath a weaker, deeper layer. The modeled sea breeze had other characteristics similar to lidar data, such as timing of onset and depth, but the onshore flow was weaker. These results imply that the dual structure of the sea-breeze flow was associated with the coastal mountain, and not with the inland mountain. As in the smoothed terrain case, the early morning offshore flow near the surface was strong, yet the vertical extent was inhibited. The major effect of the missing inland mountain was the lack of westerly, or onshore, flow above 1500 m throughout the simulation. In the absence of westerly flow above the sea-breeze layer, a 6 m s^{-1} offshore flow developed above the deep sea breeze, which was much stronger than that seen in lidar measurements, and too strong to be a compensatory sea-breeze return flow.

Dramatic differences existed in the model results shown in Fig. 12d compared to the other simulations and lidar measurements. In this simulation, the coastal mountain was removed, leaving the land–water contrast and the inland mountain as the two driving forces for the mesoscale winds. Three striking features in these results are 1) the lack of dual structure in the sea-breeze flow, 2) the strong offshore flow in the morning, and 3) the strong onshore flow above 1500 m ASL in the morning. Early morning offshore flow was deep, reaching speeds of 8 m s^{-1}. The opposing onshore flow above this was also strong, well defined, and lasted many hours. The sea-breeze flow was strong ($>$6 m s^{-1}) but shallow ($<$500 m), without the weaker and deeper onshore flow seen in the other simulations and measurements.

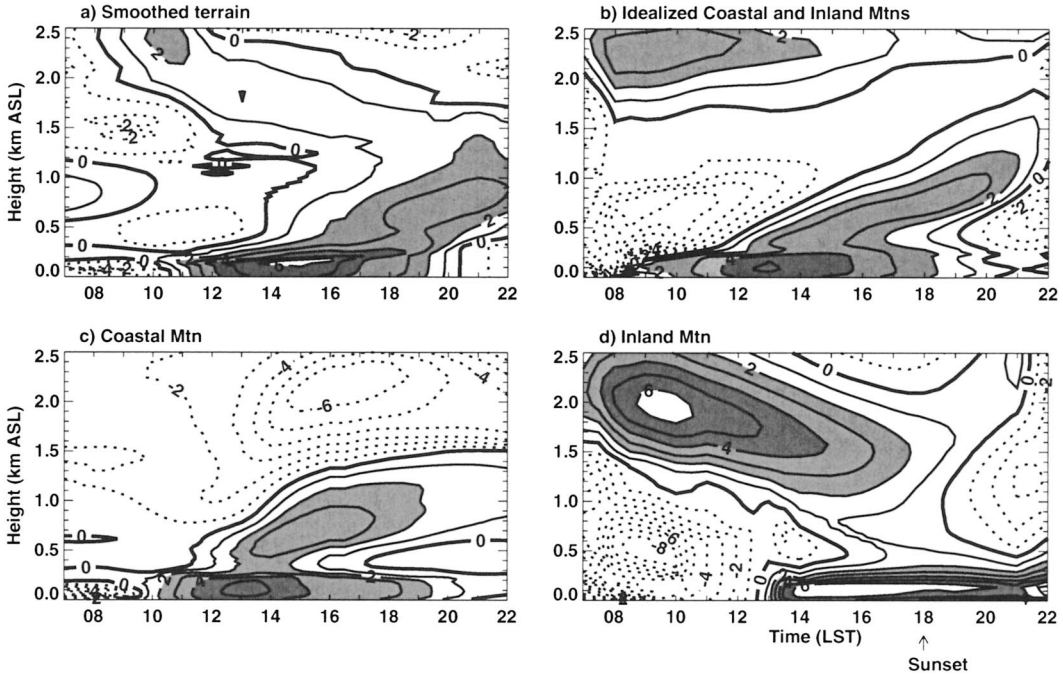

FIG. 12. Time–height series of the u component of the wind (in m s^{-1}) extracted from the shore in simulations 1–4. These simulations had water in the western portion of the domain. Profiles were extracted on the hour and half hour from 0700 to 2200 LST. Solid (positive) contours indicate westerly flow. Dashed contours indicate easterly flow. Westerly flow, 2–4 m s^{-1}, is shaded medium gray and flow, 4–6 m s^{-1}, is shaded dark gray: (a) smoothed terrain, (b) idealized dual mountain, (c) idealized coastal mountain, and (d) idealized inland mountain.

It is clear from comparing this simulation with simulations 1–3 (Figs. 12a–c) and the measurements (Fig. 5) that the presence of the inland mountain significantly affected winds above 1500 m ASL. It is also apparent that the depth of the onshore sea-breeze flow was limited without the coastal mountain, because the deep layer of onshore flow evident in the other simulations and measured by the lidar failed to form. Also, the onshore flow was stronger in the absence of the coastal range. This implies that the coastal mountain generated a slope flow that enhanced the depth of the onshore flow, but not its speed. The depth of the onshore flow generated only by the local-scale land–water contrast (Fig. 12d) was similar in depth to the shallow portion of the sea breeze in the simulations that show the dual structure in the onshore flow. This implies that the land–water contrast drove the shallow sea breeze.

When the coastal-mountain-only plot (Fig. 12c) is compared to simulations that included the inland mountain (Figs. 12a, 12b, and 12d), it is apparent that flows generated by a mountain of this size (3800 m), even 300 km inland, were a primary component of the flow above 1500 m ASL near the shore.

2) TERRAIN SENSITIVITY WITHOUT THE LAND–WATER CONTRAST

Figure 13 shows results from the simulations with short grass only in the domain. Therefore, the mesoscale wind flows generated in these simulations were due solely to the terrain. Comparing the dual-mountain results with water (Figs. 12a and 12b) to those without water (Figs. 13a and 13b) shows that the similarities between the water and no-water runs are greater above 1500 m ASL than below. This implies that the land–water contrast did not strongly influence the winds above 1500 m in these simulations. The land–water contrast did strongly influence the flow in the lower 1500 m of the domain, however, as indicated by the large differences seen in the winds between all of the water and no-water simulations. Without the cooling effect of the sea-breeze flow, the air mass west of the coastal mountain heated up much faster in the no-water simulations. Once the flow shifted from downslope to upslope, the vertical growth of the westerly flow occurred suddenly, and the ensuing westerly flow was weak and deep.

As in the dual-mountain cases, the coastal-mountain-only case (Fig. 13c) had weak and deep afternoon westerly flow, but it was stronger without the presence of the inland mountain, a characteristic also seen in the west–east cross sections. Winds above 1500 m AGL were similar in structure to the case with water (Fig. 12c). Without the coastal mountain or the land–water contrast (Fig. 13d), the afternoon westerly flow below 1500 m AGL was quite weak. Strong winds above 1500 m associated with the inland mountain appeared in the no-water simulation, as in the corresponding case with water in the domain, although they were weaker.

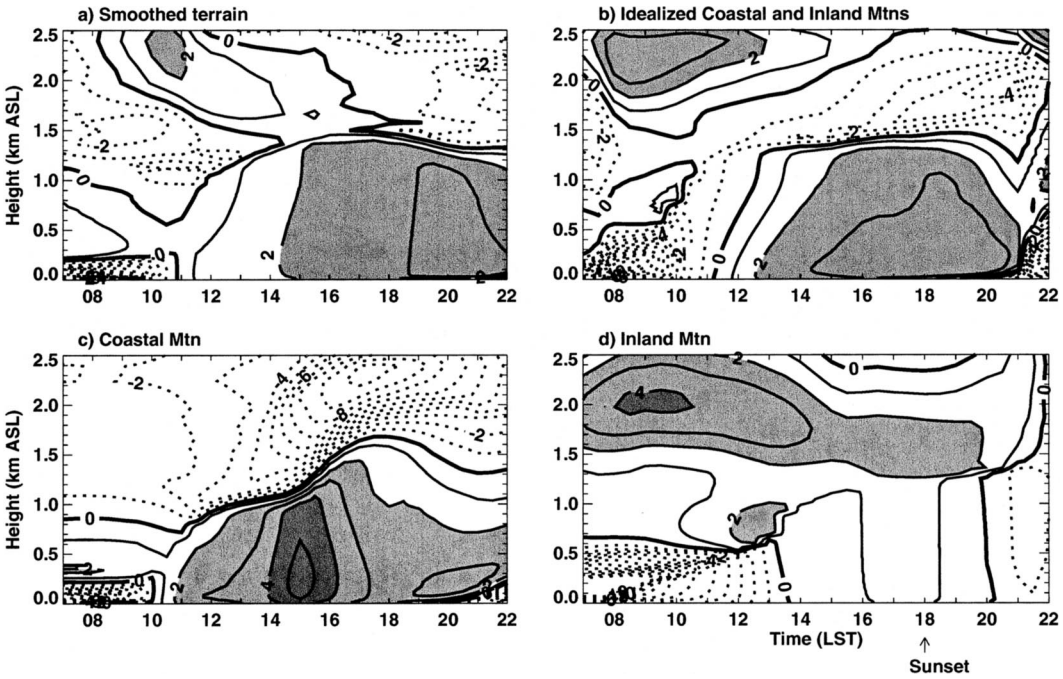

FIG. 13. As in Fig. 12 except for simulations 6–9, simulations with short grass rather than water in the western portion of the domain.

c. Thermodynamic profiles

A prominent feature of the marine boundary layer along the west coast of the United States is a strong, shallow temperature inversion. Thermodynamic profiles launched on 16 September 1987 from a research vessel, the R/V *Silver Prince* (R/V *SP*), are reproduced here from Banta et al. (1993). These profiles of virtual potential temperature, θ_v, show the change of the marine boundary layer over time (Fig. 14). The R/V *SP* was stationed 11 km directly west of Moss Landing, California. The transition to onshore flow began at ~0930 LST at the shore (Fig. 5), so the sounding launched from the R/V *SP* at 1735 UTC (0935 LST) represented pre-sea-breeze conditions at the R/V *SP*. All three soundings indicated a strong stable layer below 310 m throughout the time period.

Profiles of θ_v were extracted from grid points 18 km west of the shore from simulation 2 (idealized dual-mountain terrain with water in the western portion of the domain). Figure 15 shows the model profiles from times that closely match the times of the sounding data. The heights and strengths of the inversions in the three R/V *SP* profiles and the model profiles are shown in Table 2. With time, the error in the model inversion heights increased when compared to the soundings, with a maximum error of 98 m. The model slightly overpredicted the inversion height early, and then underpredicted it in the afternoon. The model underpredicted the inversion strength at all three times, the error growing with time.

To investigate the two scales of sea-breeze flow from a thermodynamic point of view, more profiles of θ_v were extracted from simulation 2. Profiles from the center of the valley (144 km east of the shore) and 256 km west of the shore represent the continental scale of forcing. Another profile was extracted 56 km west of the shore to compare with the profile at the shore for local-scale forcing. Figure 16 shows profiles from these locations at four different times. The early morning profiles (Fig. 16a) indicate the warmest temperatures occurred in the westernmost profile (256 km west of the shore, solid line) for most of the profile shown, while the coolest temperatures occurred at the shore and in the valley, especially near the surface. The largest temperature contrast occurred at ~500 m AGL, corresponding with the height of the strongest offshore flow (cf. thermodynamic profiles with the corresponding wind profiles shown in Fig. 12b). At 1300 LST the sea-breeze flow was well established in the lowest 500 m (Fig. 12b). The thermodynamic profiles (Fig. 16b) show that the temperature contrast between the shore profile and the profile 56 km offshore (dashed and dotted lines, respectively) indicates warmer temperatures at the coast than over the water in the lowest 300 m, thus supporting the shallower sea breeze. The larger and deeper temperature contrast between the warming valley (144 km east of the shore) and the profile 256 km offshore (dash–dot and solid lines, respectively) supported the deeper onshore flow. Figure 16c shows that by 1700 LST the valley was much warmer than the other locations in the lowest 500 m

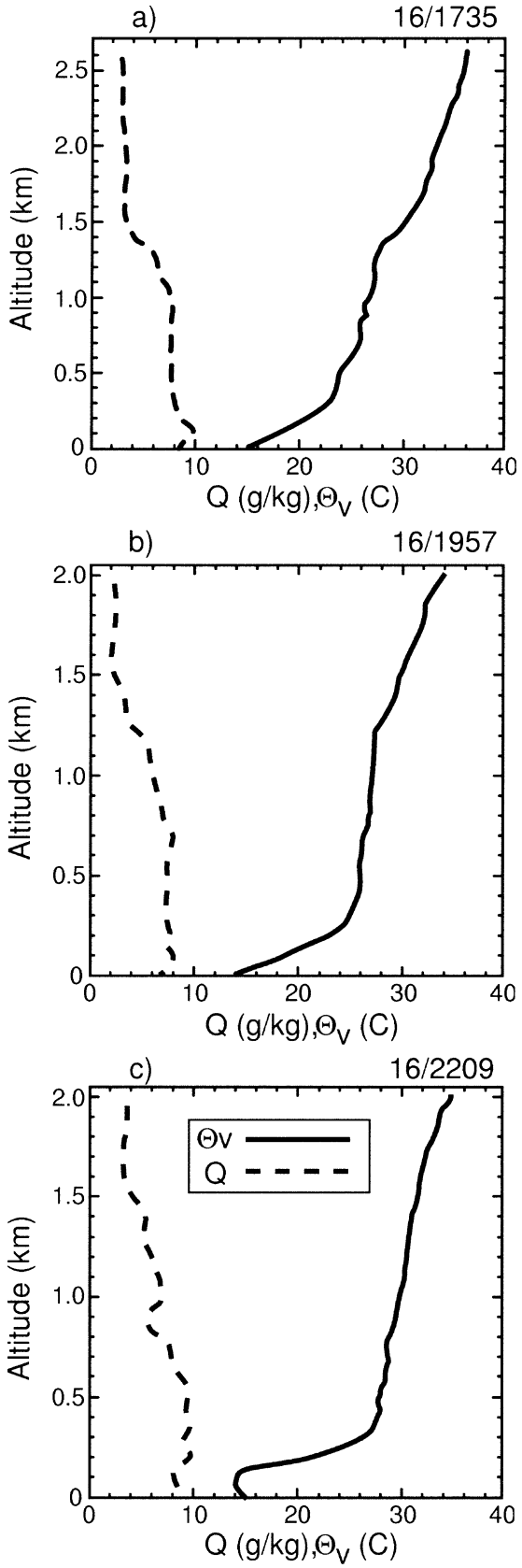

AGL, the temperature contrast continuing to maintain the deeper onshore flow. The last profiles presented (Fig. 16d, 2100 LST, 3 h after sunset) indicated that very near the surface the temperature at the shore was slightly cooler than the temperatures over the water, supporting the reversal from onshore to offshore flow seen in the wind profiles (Fig. 12b). Temperatures in the valley, while still much warmer than the other profiles, were beginning to decrease.

Overall, the model-simulated θ_v profiles indicated that the model did well in predicting the inversion height, but was less successful in simulating the inversion strength. The theory put forth in Banta (1995) that the shallow and deep sea breezes were driven by two scales of thermal forcing (local and continental) was supported by the model θ_v profiles.

5. Factor separation

a. Method

Stein and Alpert (1993) devised a straightforward method for computing the contribution of individual factors to the magnitude of a predicted field in a numerical model, and more importantly, the contribution of the interaction of two or more factors to the outcome of the simulation. It is standard among modelers to test a factor of interest by completing a simulation with and without the factor, for example, topography, and then looking at the difference in the predicted field of interest. Stein and Alpert (1993) showed that this method leads the investigator to miss the interaction that occurs between dominating factors, therefore possibly missing important driving forces for the feature of interest.

Their method is based on the idea that a field f, which is a continuous function of c, can be decomposed into a part that is independent of c and a part that is dependent on c. The function is decomposed using a Taylor series type expansion based on the number of factors to be tested, n. They showed that there must be 2^n simulations to apply the method.

In the following section we will present factor separation results for different pairs of factors, and investigate the triple interaction between the coastal mountain, the inland mountain, and the land–water contrast. The equations used, taken from Stein and Alpert (1993), are as follows:

←

FIG. 14. Radiosonde ascents from the R/V *Silver Prince* showing vertical profiles of virtual potential temperature (θ_v) and specific humidity (q) for 16 Sep 1987. (a) A strong stable layer persisted below 300 m above the sea surface at 1735 UTC (0935 LST). (b) The same stable layer is observed at 1957 UTC (1157 LST). (c) A shallow mixed layer has formed in the lower half of the inversion layer by 2209 UTC (1409 LST). [Reproduced from Banta et al. (1993).]

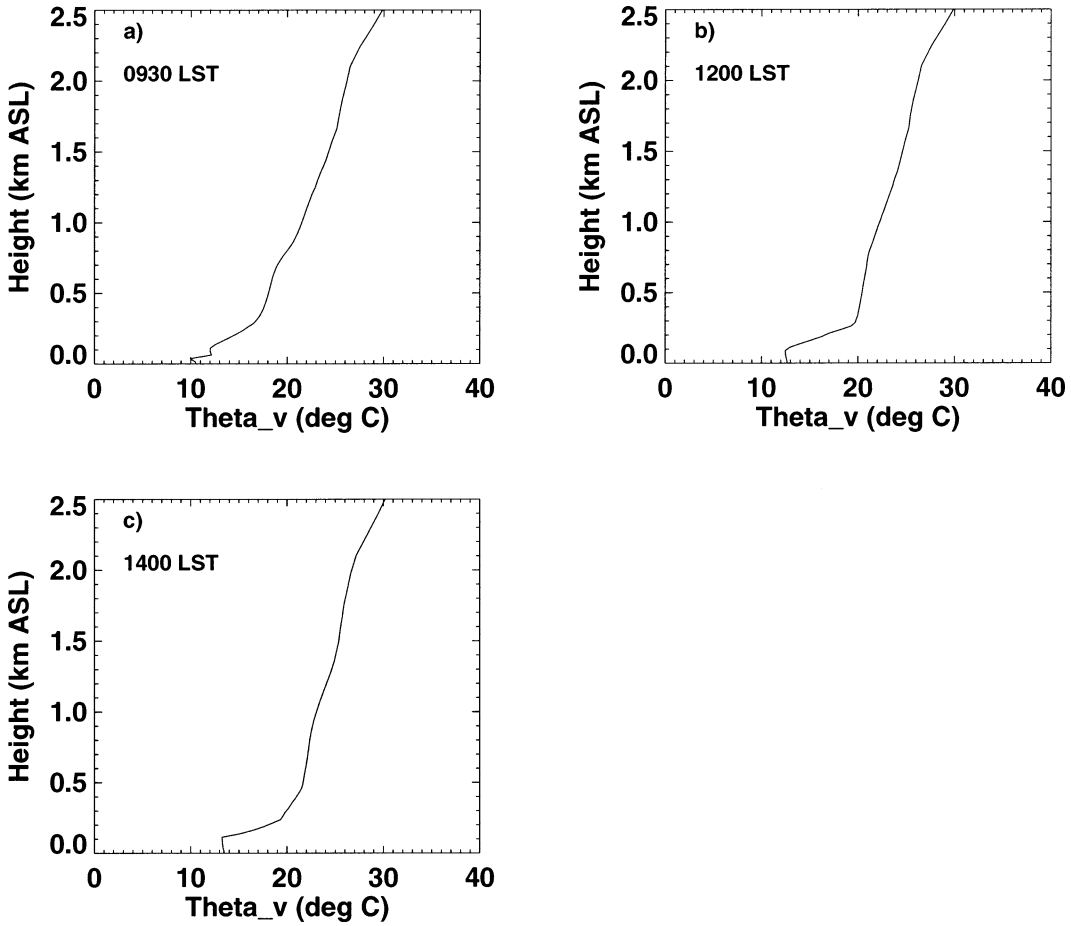

FIG. 15. Profiles of θ_v extracted from simulation 2. The profiles were taken from grid points 18 km west of the shoreline: (a) 0930 LST (1730 UTC); (b) 1200 LST (2000 UTC), and (c) 1400 LST (2200 UTC).

$$\hat{f}_0 = f_0, \tag{1}$$

$$\hat{f}_1 = f_1 - f_0, \tag{2}$$

$$\hat{f}_2 = f_2 - f_0, \tag{3}$$

$$\hat{f}_3 = f_3 - f_0, \tag{4}$$

$$\hat{f}_{12} = f_{12} - (f_1 + f_2) + f_0, \tag{5}$$

$$\hat{f}_{23} = f_{23} - (f_2 + f_3) + f_0, \tag{6}$$

$$\hat{f}_{13} = f_{13} - (f_1 + f_3) + f_0, \quad \text{and} \tag{7}$$

$$\hat{f}_{123} = f_{123} - (f_{12} + f_{23} + f_{13}) + (f_1 + f_2 + f_3) - f_0. \tag{8}$$

In each equation, $\hat{f}$, the fraction of f that is due to the factor or factors under investigation, is calculated from the model output, f, where f is a model-variable field, such as u, θ, etc. Equations (5)–(7) are for testing pairs of factors, while (8) is for testing a triple interaction.

If two factors to be investigated are topography and the land–water contrast, and the predicted field of interest, f, is the u component of the wind, then (1) represents the simulation that does not include topography or a land–water contrast, and shows the influence on f of the ''hidden'' factors, that is, the factors not under consideration. In (2), the effects of topography are isolated. A simulation is run with topography, but no land–water contrast, creating the wind field f_1. When the hidden factors, f_0, are subtracted from f_1, we get $\hat{f}_1$, the u component of the wind as a result of topography only. Likewise, in (3), the u component of the wind as a result of the land–water contrast only is calculated, $\hat{f}_2$.

The final step for testing a pair of factors is to retrieve the field of interest due to the interaction of two factors, $\hat{f}_{12}$. Starting with the simulation that has both factors present, subtract the results due to the hidden factors and the factors of interest individually:

$$\hat{f}_{12} = f_{12} - \hat{f}_0 - \hat{f}_1 - \hat{f}_2. \tag{9}$$

Using the right-hand side of (1)–(3) to substitute for the $\hat{f}$ terms results in (5). Large values of $\hat{f}_{12}$, calculated from (5), represent regions where the interaction between the two fields is strong. All equations listed are similarly used to test a triple interaction.

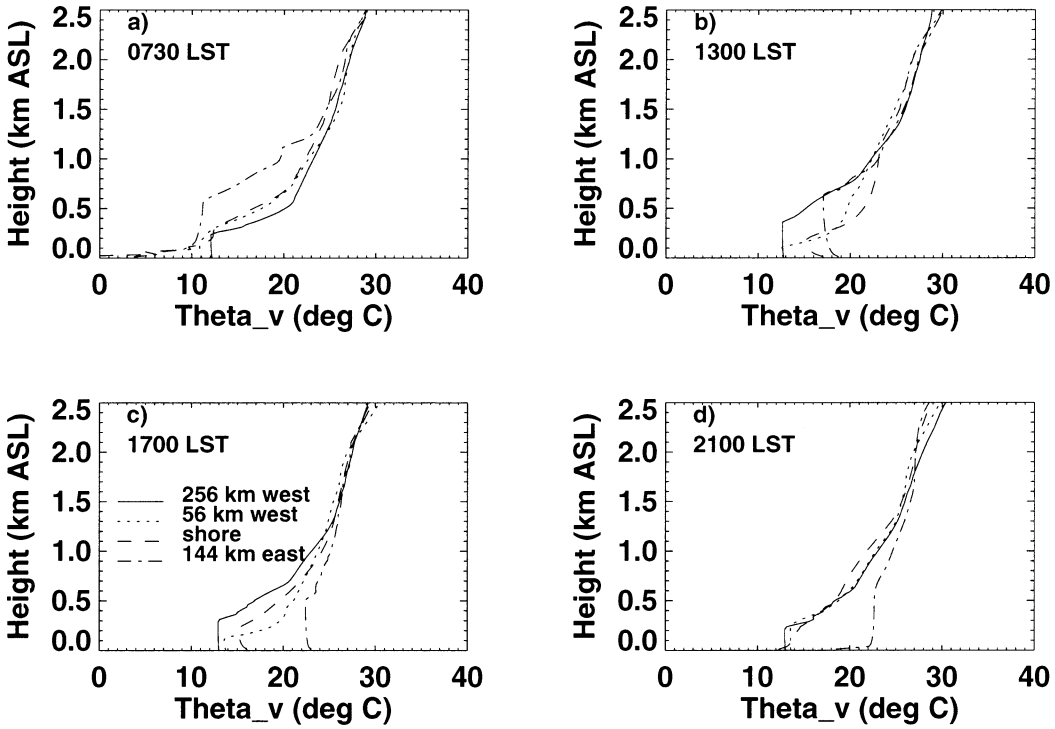

FIG. 16. Profiles of θ_v extracted from the domain of simulation 2 from four different locations. Solid lines indicate profiles from grid points 256 km west of the shoreline, dotted lines are for profiles 56 km west of the shoreline, dashed lines represent profiles taken from the shoreline, and the dashed–dotted lines represent profiles taken from the center of the valley (144 km east of the shoreline): (a) 0730, (b) 1300, (c) 1700, and (d) 2100 LST.

b. Factor separation results

In this section we present the factor-separation results for three pairs of factors: 1) coastal (f_1) and inland (f_2) mountains (land–water contrast not included), 2) coastal (f_1) and inland (f_2) mountains (land–water contrast included), and 3) idealized dual-mountain topography (f_1) and land–water contrast (f_2). The figures presented include west–east cross sections of f_0, f_1, f_2, f_{12}, and $\hat{f}_{12}$, as explained in the previous section. To fully understand the plot illustrating the wind flow as a result of the interaction of the factors, $\hat{f}_{12}$, there are three things to look for. 1) Where is $\hat{f}_{12} = 0$? The interaction of factors has no effect on f, the u component of the wind, where $\hat{f}_{12} = 0$. 2) Where are the regions of greatest magnitude of $\hat{f}_{12}$? These are the places where the interaction has the most effect. 3) What is the sign of these regions of greatest magnitude relative to the simulation including both factors? If the sign in $\hat{f}_{12}$ is the same as in the corresponding region of f_{12}, then the interaction of the two factors enhanced the flow modeled in f_{12}; if the sign is opposite, then the interaction of factors opposed, that is, weakened, the modeled flow. Time–height series of $\hat{f}_{12}$ for the three factor pairs are also shown. In addition, a time–height series plot of $\hat{f}_{123}$, the winds as a result of the triple interaction among the coastal mountain, the inland mountain, and the land–water contrast, is shown.

TABLE 2. Comparison between inversion height and inversion strength as measured from soundings launched from the R/V *Silver Prince* on 16 Sep 1987 and as modeled in simulation 2. The first column indicates time (LST), the second column has inversion heights and strengths as indicated by the model, the third column has inversion heights and strengths from the soundings, and in the last column, the observations were subtracted from the simulation.

Time (LST)	Model inversion height (m)	R/V *SP* inversion height (m)	Model − R/V *SP* (m)
0930	300	290	10
1200	287	250	37
1400	212	310	−98
Time (LST)	Model inversion strength (°C)	R/V *SP* inversion strength (°C)	Model − R/V *SP* (°C)
0930	6.5	8	−1.5
1200	6.5	11	−4.5
1400	6.0	12	−6.0

The results for the coastal mountain (f_1) and the inland mountain (f_2) factor pair, without water included in the domain, are shown in Fig. 17. It is interesting how much weaker the coastal-mountain slope flows were when the inland mountain was present (cf. Fig. 17b with Fig. 17d). Since the coastal-mountain slope flows were much stronger in f_1 than in f_{12} (and winds in the same region were negligible in f_0 and f_2), the winds due to the interaction of the mountain-induced

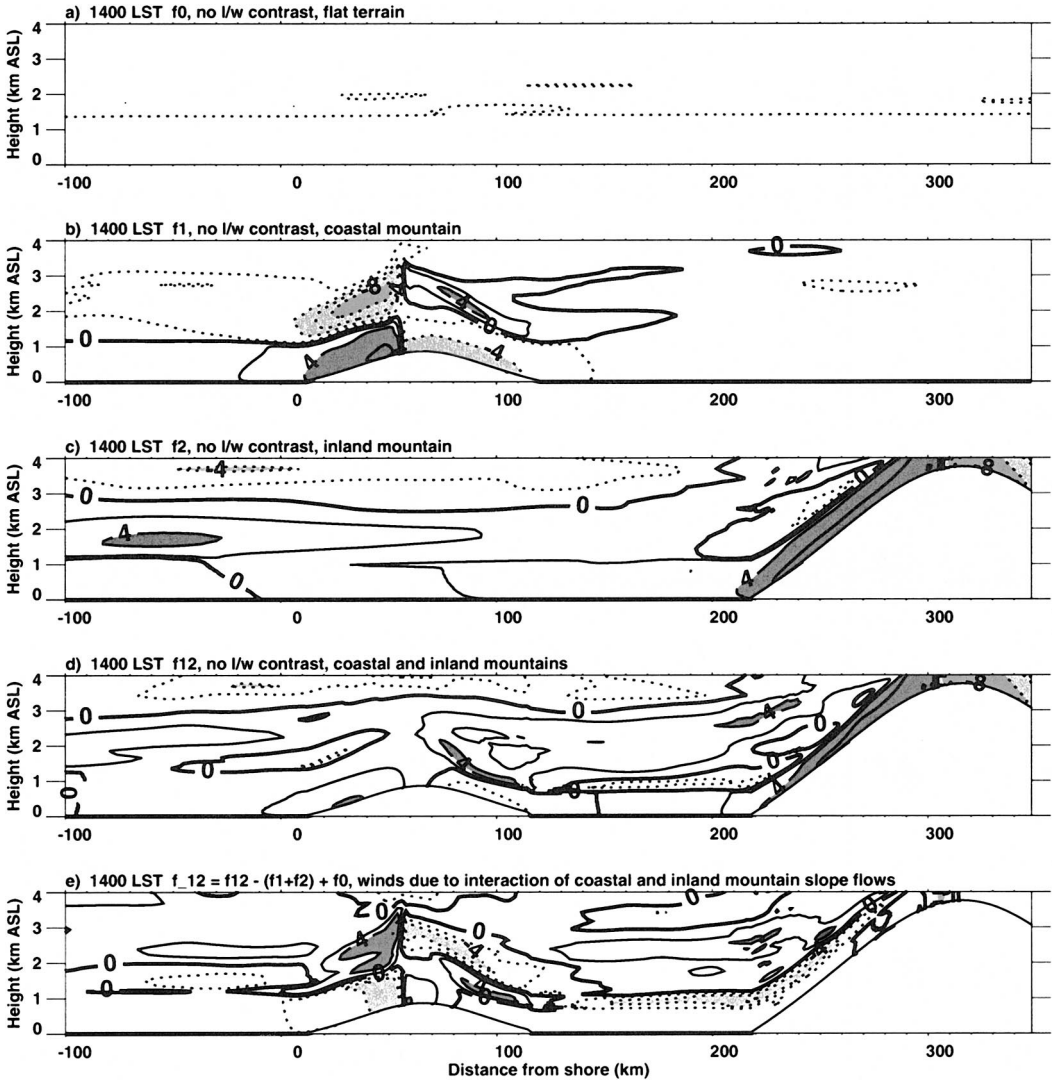

FIG. 17. West–east cross sections of the modeled u component of the wind. Solid (positive) contours indicate westerly flow, and increment every 2 m s^{-1}, except in the flat terrain plot, (a), which has 1 m s^{-1} increments. Speeds greater than 4 m s^{-1} are shaded dark gray. Dashed (negative) contours indicate easterly flow, with speeds of magnitude greater than 4 m s^{-1} shaded light gray. The first four panels are from the same time, 1400 LST, but for different simulations, as indicated by the terrain (very light shading). The bottom panel shows the winds as a result of the factor-separation method employed. The factor pair assessed in this figure is the coastal mountain and the inland mountain, with no water in the domain: (a) f_0, neither mountain in the domain; (b) f_1, coastal mountain only; (c) f_2, inland mountain only; (d) f_{12}, both mountains, and (e) $\hat{f}_{12}$, the winds due to the interaction of the flows induced by both the coastal and the inland mountains.

flows, $\hat{f}_{12}$ (Fig. 17e), were opposite in sign to the coastal-mountain solenoidal flow (Fig. 17d), except for a small region of westerly flow at $x = 80$–110 km and $z = \sim 1$ km. This signified that, for the most part, the interaction of flows induced by both mountains together opposed the coastal-mountain solenoidal flow.

Figure 18 shows plots for the coastal mountain (f_1) and the inland mountain (f_2) factor pair with the land–water contrast included. In this case, only the upslope flow on the east side of the coastal mountain was weaker when the inland mountain was present. The interaction of the slope-induced flows of both mountains (Fig. 18e) enhanced the sea breeze/slope flow on the western side of the coastal range, except near the leading edge of the sea breeze where this interaction opposed the advance of the leading edge of the sea breeze. The interaction also enhanced the return flow for the sea breeze/slope flow. Both of these effects, at this time, were in contrast to the previous factor pair. Even with the return-flow enhancement, however, the sea-breeze return flow modeled in f_{12} (Fig. 18d) was nearly nonexistent. Note that the modeled winds on the east side of the coastal mountain (and the interaction of flows results) were quite similar to the results in the previous factor pair, indi-

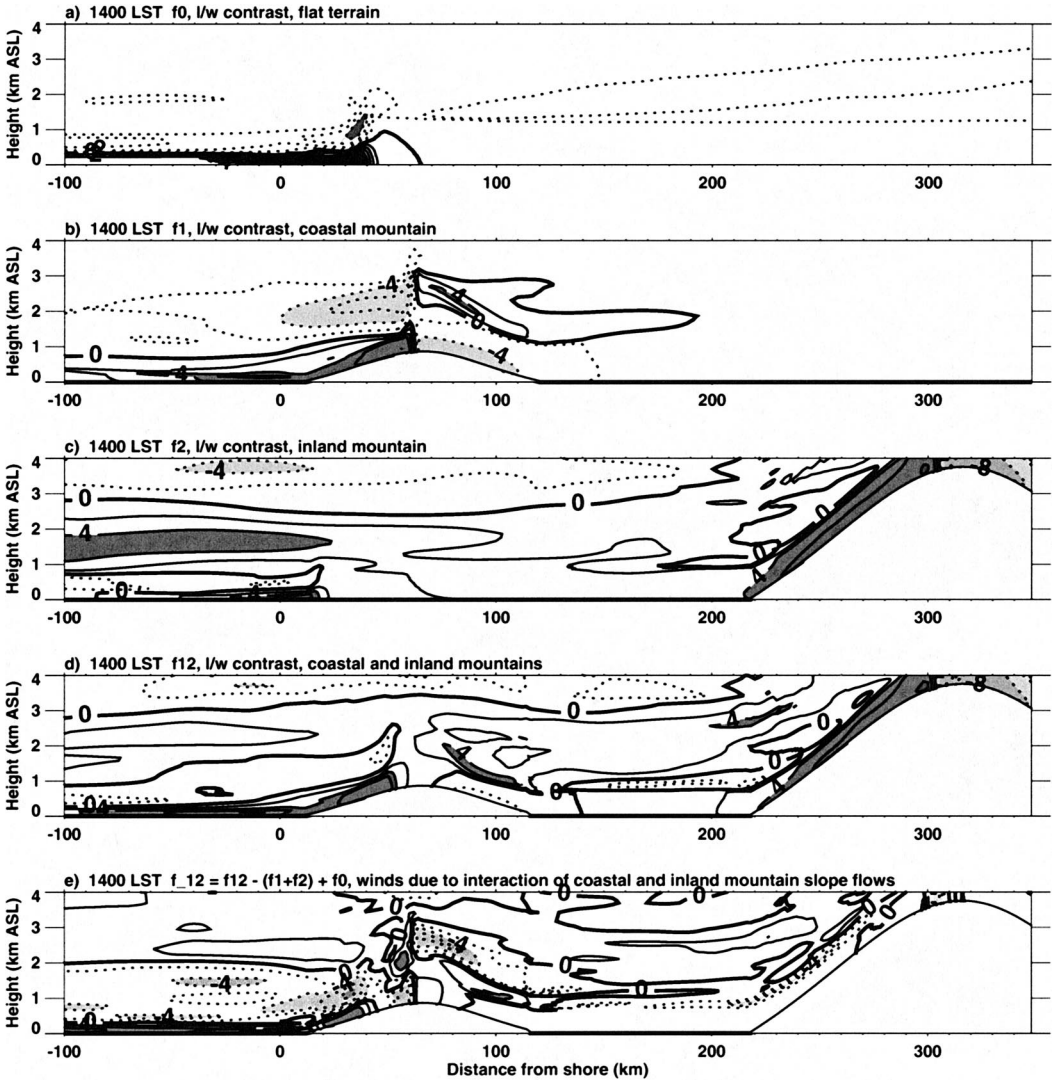

FIG. 18. As in Fig. 17 but the factor pair is the coastal and the inland mountains, with water in the western portion of the domain.

cating that the presence of water in the western portion of the domain did not affect the winds east of the crest of the coastal mountain at this time. The comparison of these results with those of the previous factor pair indicates that the presence of the sea breeze reversed the influence of the interaction of the mountain flows on the western slope of the coastal mountain and to its west.

Figure 19 shows plots for the idealized dual-mountain topography (f_1) and land–water contrast (f_2) factor pair. Figure 19e, $\hat{f}_{12}$, shows that the interaction of these two factors had very little influence on f east of the crest of the coastal mountain. The affected region was from the crest of the coastal mountain ($x = 65$ km) westward, mostly in the lowest few hundred meters above the surface. Where the values were negative (dashed lines), the interaction between the slope and land–water contrast opposed the modeled surface flow on the western slope of the coastal mountain and over the water (cf. f_{12} to $\hat{f}_{12}$, Figs. 19d and 19e, respectively). Just behind the leading edge of the combined sea breeze/slope flow, however, a slight augmentation of the westerly flow is evident for $x = 40$–50 km. With time, this enhancement at the leading edge of the sea breeze weakened or reversed (Fig. 20c).

Figure 20 shows time–height plots of $\hat{f}_{12}$ for the three cases discussed, and the triple interaction results, $\hat{f}_{123}$. The profiles were extracted from the shore, and illustrate the impact of the interaction of the factor pairs at the shore over time. In the case of the coastal and inland mountains with no water in the domain (Fig. 20a) the influence of the interaction of the slope flows near the surface occurred only in the morning and well after sunset. In the morning, the interaction acted to enhance onshore flow (dark gray shading) until 0900 LST. Dur-

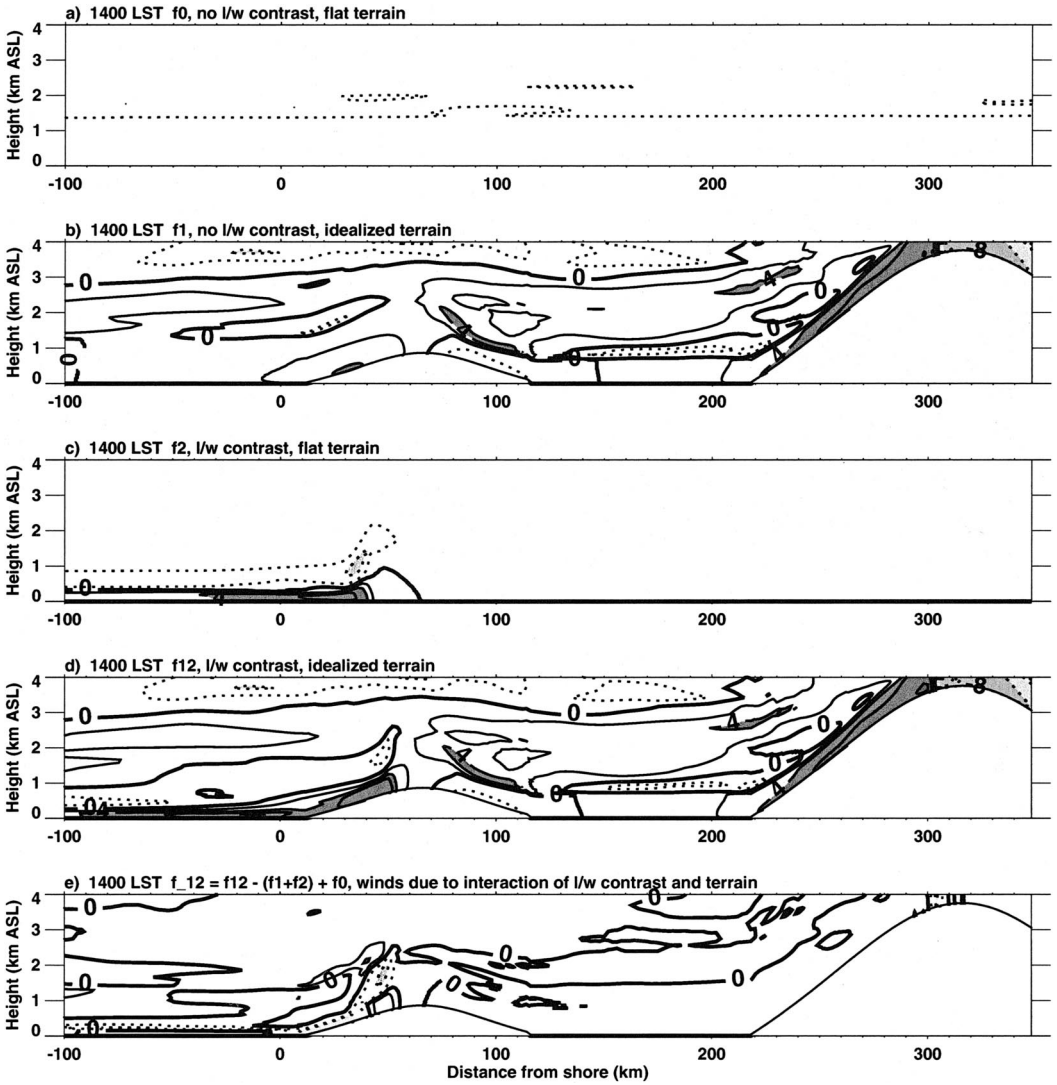

FIG. 19. As in Fig. 17 but the factor pair is the land–water contrast and the idealized dual-mountain terrain: (a) f_0, neither mountain nor water in the domain; (b) f_1, both mountains, no water; (c) f_2, flat terrain, with water; (d) f_{12}, both mountains; and (e) $\hat{f}_{12}$, the winds due to the interaction of the flows induced by the land–water contrast and the terrain.

ing the rest of the morning and afternoon, the influence at the surface was very weak. In the evening, the interaction of the slope flows worked to enhance the offshore flow at the surface (light gray shading). The most significant effect of the interaction above 1.5 km ASL was during the afternoon and early evening hours.

When water was added to the domain, Fig. 20b, the promotion of westerly flow in the morning extended for several more hours, and had an even stronger effect than the case without water. After 1300 LST the effect was still to enhance westerly flow below 500 m, but very weakly. Above 500 m in the afternoon and early evening, easterly flow was enhanced, and then westerly flow above 2 km was enhanced.

As in the $\hat{f}_{12}$ panels of the west–east cross sections, the interaction between the terrain-induced flows and the land–water contrast flows opposed the sea-breeze flow in the late afternoon and early evening (Fig. 20c). The strongest enhancement of the onshore surface flow was from 0800 to 1000 LST, with the onshore flow slightly augmented in a shallow layer. The augmentation of the morning sea breeze (dark gray shading) was weaker than in the mountain–flow interaction factor pair. During the sea-breeze development phase (1000 to 1400 LST), however, the influence was quite weak. From 1400 LST on, the interaction of the land–water contrast and the slope flows worked to oppose the sea-breeze flow (light gray shading), particularly after sunset, in agreement with Kondo's (1990) findings that the sea breeze was enhanced in the morning and opposed in the afternoon when terrain was present. Above 500 m, it was only after sunset that the interaction had a major

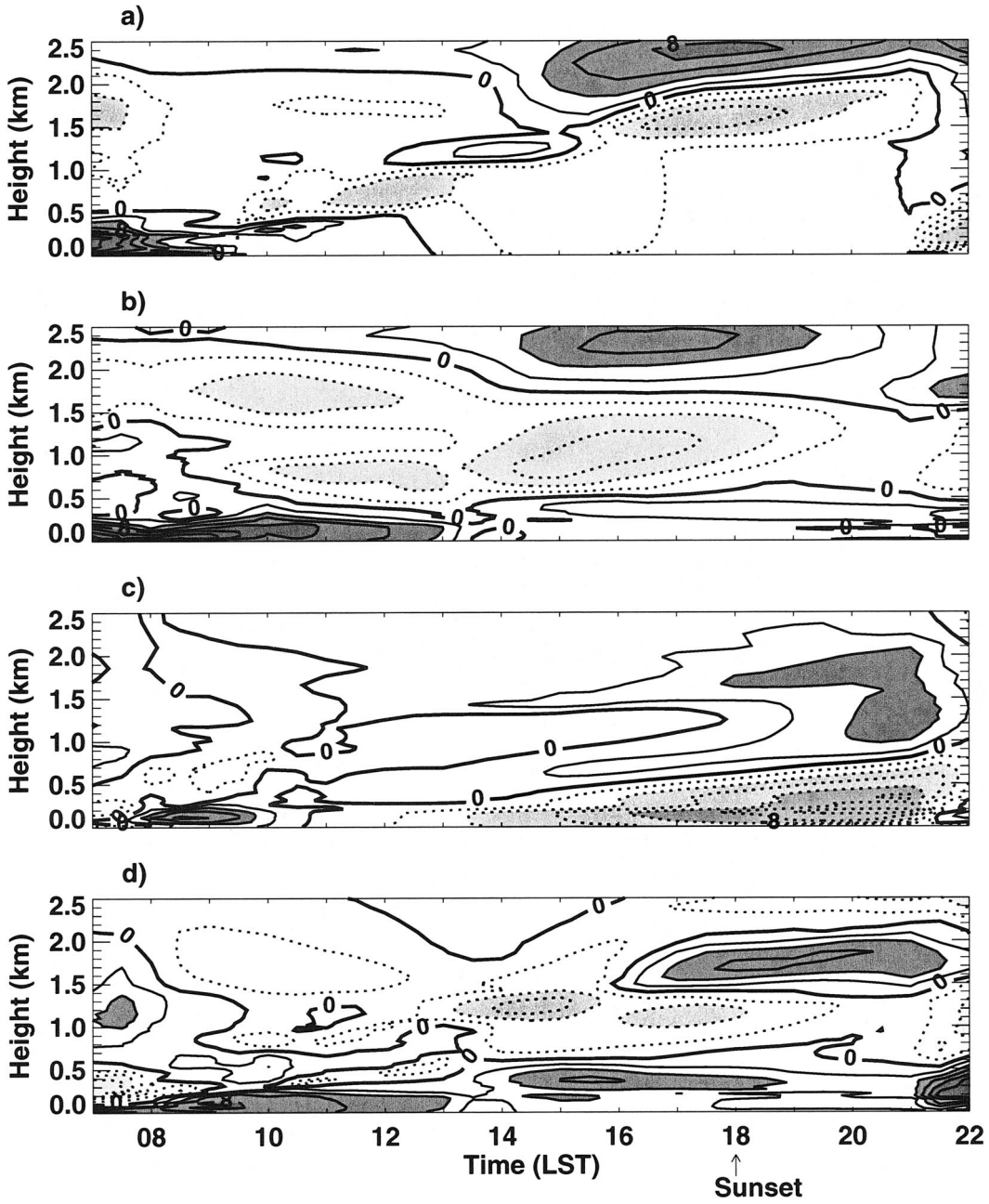

FIG. 20. Time–height cross section of the calculated $\hat{f}_{12}$ field for the three factor pair cases presented and $\hat{f}_{123}$, the triple interaction. Solid contours represent westerly flow; dashed contours represent easterly flow. Dark gray shades (westerly flow greater than 4 m s^{-1}) show where westerly flow was enhanced by the interactions. Light gray (easterly flow greater than 4 m s^{-1}) indicate where easterly flow was enhanced by the interactions. (a) Flow due to the interaction of mountain-induced flows, no water in the domain. (b) Flow due to the interaction of mountain-induced flows, with water in the domain. (c) Flow due to the interaction of the flows due to the land–water contrast and the terrain. (d) Flow due to the triple interaction of the coastal mountain, the inland mountain, and the land–water contrast.

contribution at the shore. The results below 500 m ASL for the factor pairs with water in the domain (Figs. 20b and 20c) show that the interaction of mountain flows dominated in the morning (enhancing the sea-breeze flow), whereas the interaction of the land–sea contrast and sloping terrain dominated in the afternoon (opposing the sea-breeze flow and enhancing the return to offshore flow after sunset).

The effects of the triple interaction among the coastal mountain, the inland mountain, and the land–water contrast are shown in Fig. 20d. Except for the first 1.5 h depicted in the morning (0700–0830 LST),

the interaction below 500 m ASL enhanced the onshore flow. The development of the shallow sea breeze was strongly enhanced at ~0900 LST, which corresponded to the time of sea-breeze onset seen in Fig. 12b (the time–height series of *u* from the simulation that included all three factors). After 1400 LST, the enhancement was elevated ~300 m from earlier in the day, corresponding to the onset of the deeper portion of the sea breeze.

6. Summary

The NOAA/ETL Doppler lidar deployed at Monterey Bay in September 1987 successfully measured the vertical structure of the sea breeze with high spatial-resolution scans perpendicular to the shore (Banta et al. 1993; Banta 1995). The complex terrain surrounding the Monterey Bay area causes the sea breeze to be more complex than predicted by theory, and the structure is highly three-dimensional. Nearly horizontal lidar scans show the horizontal variability near the coast quite well. Nevertheless, the lidar cross sections perpendicular to the coast yield much information about the vertical structure of the Monterey Bay sea breeze, and a careful study of the evolution of this vertical structure led to a conceptual model of the onshore flow in which sea-breeze forcing occurred on two length scales, a local scale between the ocean and the coastal mountains, and a larger scale from the sea to the taller inland mountains. This model implies that the dominant forcing that drives the two scales of onshore flow is 2D, and in this study we have employed a 2D mesoscale numerical model to assess this conclusion. The Doppler lidar provided the time history of the vertical structure of the onshore flow component, and using this information to assess model performance is a good starting point for numerically investigating the sea breeze.

The time–height plots of the RAMS modeled *u* component of the wind in the dual-mountain simulations replicated many of the key features seen in the lidar measurements (Fig. 5), particularly the shallow and deep onshore flow. As expected, the inclusion of both the coastal and inland mountain ranges in the model domain yielded the most realistic results (Figs. 12a and 12b). The slope flows generated by each mountain influenced the structure of the sea-breeze flow near the surface and the expected return flow above the sea-breeze layer. The coastal mountain generated a weak slope flow ~1500 m deep, producing the larger-scale onshore flow seen in the lidar sea-breeze measurements. The land–water contrast was responsible for the shallow sea breeze. The presence of the inland mountain, representing the Sierra Nevada range, greatly influenced the flow above 1500 m ASL by generating westerly flow above 1500 m ASL. Since simulations with the inland mountain produced westerly flow above 1500 m and simulations without it had easterly flow at these heights, this topographic feature clearly affected winds near the shore even though it was hundreds of kilometers inland. In this 2D setting, the westerly flow above 1500 m ASL associated with the inland mountain hindered the development of a classic sea-breeze return flow.

Model results were most realistic in the lowest 1500 m of the domain. Low-angle conical lidar scans indicated that the onshore flow was most likely to be perpendicular to the shore at the lowest levels (Fig. 2), and therefore the lower-level winds were more likely to be successfully reproduced in a 2D model domain that was perpendicular to the shore. Lidar data indicate that with time, the wind direction did change with height, and the winds above the surface were not always perpendicular to the shore. Two-dimensional simulations could not account for these changes, particularly above 1500 m AGL, where the agreement between lidar and RAMS simulations was less successful.

Factor separation results for the idealized dual-mountain sea-breeze simulation showed that the interaction between the coastal and the inland mountains was a dominating force in the morning hours, enhancing the onshore flow (Fig. 20). The interaction between terrain and the land–water contrast was a strong force in the afternoon, opposing the sea-breeze flow. Whereas the coastal-mountain slope flow acted to enhance the sea-breeze flow, particularly in the morning, the mountain also acted as a barrier to the sea breeze, impeding its progress in the afternoon. The triple interaction among the coastal and the inland mountains and the land–water contrast worked to enhance onshore flow at the surface for the entire time period analyzed (0700–2200 LST). However, this enhancement became quite weak in the afternoon when the opposing effects due to the interaction of the land–water contrast and terrain became very strong.

The results of the interactions above the sea-breeze layer, where the expected return flow would be, were not free from ambiguity. The triple interaction and the interaction of the mountain flows acted to promote easterly flow from 500 to 1500 m AGL in the afternoon, yet only very weak easterly flow was seen at this time in the dual-mountain simulations. The factor separation results did not explain the early morning westerly flow above 2 km either, although in the time–height series comparison this flow was clearly associated with the inland mountain.

Overall we note that the 2D numerical model was successful in reproducing the essential aspects of the flow across the shore as measured by the Doppler lidar. The two scales of onshore flow were even more evident in the model simulations than in the measurements. This success, as well as the large differences between the dual-mountain and single-mountain cases, imply that the 2D forcing due to the two parallel mountain ranges represented in the model is capable of producing the temporal behavior of the flow at the shore. In the real case, of course, 3D effects could still have a significant in-

fluence on the evolution of these coastal flow systems. Our purpose here was to show that 2D effects could explain the observed behavior.

Acknowledgments. The authors wish to thank Richard Cupp and the rest of the lidar crew that worked to obtain the lidar data during LASBEX. Drs. Cathy Finley, Gregory Poulos, Graham Feingold, and Robert Walko all gave valuable advice regarding the RAMS simulations. Helpful reviews of the manuscript were received by Janet Intrieri, Brad Orr, and two anonymous reviewers. We also wish to thank Dr. Richard Johnson for helpful discussions regarding the sea breeze in complex terrain.

REFERENCES

Arritt, R. W., 1987: The effect of water surface temperature on lake breezes and thermal internal boundary layers. *Bound.-Layer Meteor.,* **40,** 101–125.

Atkinson, B. W., 1981: *Mesoscale Atmospheric Circulations.* Academic Press, 495 pp.

Avissar, R., and R. A. Pielke, 1989: A parameterization of heterogeneous land surfaces for atmospheric numerical models and its impact on regional meteorology. *Mon. Wea. Rev.,* **117,** 2113–2136.

——, M. D. Moran, G. Wu, R. N. Meroney, and R. A. Pielke, 1990: Operating ranges of mesoscale numerical models and meteorological wind tunnels for the simulation of sea and land breezes. *Bound.-Layer Meteor.,* **50,** 227–275.

Banta, R. M., 1995: Sea breezes shallow and deep on the California coast. *Mon. Wea. Rev.,* **123,** 3614–3622.

——, L. D. Olivier, and D. H. Levinson, 1993: Evolution of the Monterey Bay sea-breeze layer as observed by pulsed Doppler lidar. *J. Atmos. Sci.,* **50,** 3959–3982.

——, and Coauthors, 1997: Nocturnal cleansing flows in a tributary valley. *Atmos. Environ.,* **31,** 2147–2162.

——, L. S. Darby, P. Kaufman, D. H. Levinson, and C. J. Zhu, 1999: Wind flow patterns in the Grand Canyon as revealed by Doppler lidar. *J. Appl. Meteor.,* **38,** 1069–1083.

Carroll, J. J., 1989: Analysis of airborne Doppler lidar measurements of the extended California sea breeze. *J. Atmos. Oceanic Technol.,* **6,** 820–831.

Chen, Y., and J. Li, 1995: Characteristics of surface airflow and pressure patterns over the island of Taiwan during TAMEX. *Mon. Wea. Rev.,* **123,** 695–716.

Clappier, A., and Coauthors, 2000: Effect of sea breeze on air pollution in the greater Athens area. Part I: Numerical simulations and field observations. *J. Appl. Meteor.,* **39,** 546–562.

Cui, Z., M. Tjernstrom, and B. Grisogono, 1998: Idealized simulations of atmospheric coastal flow along the central coast of California. *J. Appl. Meteor.,* **37,** 1332–1363.

Darby, L. S., W. D. Neff, and R. M. Banta, 1999: Multiscale analysis of a meso-β frontal passage in the complex terrain of the Colorado Front Range. *Mon. Wea. Rev.,* **127,** 2062–2081.

Doyle, J. D., 1997: The influence of mesoscale orography on a coastal jet and rainband. *Mon. Wea. Rev.,* **125,** 1465–1488.

Eastman, J. L., R. A. Pielke, and W. A. Lyons, 1995: Comparison of lake-breeze model simulations with tracer data. *J. Appl. Meteor.,* **34,** 1398–1418.

Estoque, M. A., 1962: The sea breeze as a function of the prevailing synoptic situation. *J. Atmos. Sci.,* **19,** 244–250.

Fosberg, M. A., and M. J. Schroeder, 1966: Marine air penetration in central California. *J. Appl. Meteor.,* **5,** 573–589.

Frenzel, C. W., 1962: Diurnal wind variations in central California. *J. Appl. Meteor.,* **1,** 405–412.

Intrieri, J. M., C. G. Little, W. J. Shaw, R. M. Banta, P. A. Durkee, and R. M. Hardesty, 1990: The Land/Sea Breeze Experiment (LASBEX). *Bull. Amer. Meteor. Soc.,* **71,** 656–664.

Johnson, A., Jr., and J. J. O'Brien, 1973: A study of an Oregon sea breeze event. *J. Appl. Meteor.,* **12,** 1267–1283.

Johnson, R., and R. F. Bresch, 1991: Diagnosed characteristics of precipitation systems over Taiwan during the May–June 1987 TAMEX. *Mon. Wea. Rev.,* **119,** 2540–2557.

Kimura, F., and T. Kuwagata, 1993: Thermally induced wind passing from plain to basin over a mountain range. *J. Appl. Meteor.,* **32,** 1538–1547.

Kitada, T., K. Okamura, and S. Tanaka, 1998: Effects of topography and urbanization on local winds and thermal environment in the Nohbi Plain, coastal region of central Japan: A numerical analysis by mesoscale meteorological model with a κ-ϵ turbulence model. *J. Appl. Meteor.,* **37,** 1026–1046.

Klemp, J. B., and R. B. Wilhelmson, 1978a: The simulation of three-dimensional convective storm dynamics. *J. Atmos. Sci.,* **35,** 1070–1096.

——, and ——, 1978b: Simulations of right- and left-moving storms produced through storm splitting. *J. Atmos. Sci.,* **35,** 1097–1110.

Kolev, I., O. Parvanov, B. Kaprielov, E. Doney, and D. Ivanov, 1998: Lidar observations of sea-breeze and land-breeze aerosol structure on the Black Sea. *J. Appl. Meteor.,* **37,** 982–995.

——, T. Skakalova, and I. Grigorov, 2000: Lidar measurement of the aerosol extinction profile in Black Sea coastal zone. *Atmos. Environ.,* **34,** 3813–3822.

Kondo, H., 1990: A numerical experiment on the interaction between sea breeze and valley wind to generate the so-called ''extended sea breeze.'' *J. Meteor. Soc. Japan,* **68,** 435–446.

Kotroni, V., G. Kallos, K. Lagouvardos, M. Varinou, and R. Walko, 1999: Numerical simulations of the meteorological and dispersion conditions during an air pollution episode over Athens, Greece. *J. Appl. Meteor.,* **38,** 432–447.

Louis, J. F., 1979: A parametric model of vertical eddy fluxes in the atmosphere. *Bound.-Layer Meteor.,* **17,** 187–202.

Lu, R., and R. P. Turco, 1994: Air pollutant transport in a coastal environment. Part I: Two-dimensional simulations of sea-breeze and mountain effects. *J. Atmos. Sci.,* **51,** 2285–2308.

Lyons, W. A., and L. E. Olsson, 1973: Detailed mesometeorological studies of air pollution dispersion in the Chicago lake breeze. *Mon. Wea. Rev.,* **101,** 387–403.

Mahrer, Y., and R. A. Pielke, 1977: The effects of topography on sea and land breezes in a two-dimensional numerical model. *Mon. Wea. Rev.,* **105,** 1151–1162.

McKendry, I., 1992: Numerical simulation of sea breeze interactions over the Auckland region, New Zealand. *N. Z. J. Geol. Geophys.,* **35,** 9–20.

Murayama, T., H. Okamoto, N. Kaneyasu, H. Kamataki, and K. Miura, 1999: Application of lidar depolarization measurement in the atmospheric boundary layer: Effects of dust and sea-salt particles. *J. Geophys. Res.,* **104,** 31 781–31 792.

Nakane, H., and Y. Sasano, 1986: Structure of a sea-breeze front as revealed by a scanning lidar observation. *J. Meteor. Soc. Japan,* **64,** 787–792.

Ookouchi, Y., M. Uryu, and R. Sawada, 1978: A numerical study on the effects of a mountain on the land and sea breezes. *J. Meteor. Soc. Japan,* **56,** 368–385.

Pielke, R. A., 1974: A three-dimensional numerical model of the sea breeze over south Florida. *Mon. Wea. Rev.,* **102,** 115–139.

——, 1984: *Mesoscale Meteorological Modeling.* Academic Press, 612 pp.

Post, M. J., and R. E. Cupp, 1990: Optimizing a pulsed Doppler lidar. *Appl. Opt.,* **29,** 4145–4158.

Simpson, J. E., 1994: *Sea Breeze and Local Winds.* Cambridge University Press, 234 pp.

Skinner, T., and N. Tapper, 1994: Preliminary sea breeze studies over Bathurst and Melville Islands, Northern Australia, as part of the Island Thunderstorm Experiment (ITEX). *Meteor. Atmos. Phys.,* **53,** 77–94.

Stein, U., and P. Alpert, 1993: Factor separation in numerical simulations. *J. Atmos. Sci.*, **50,** 2107–2115.

Tremback, C. J., and R. Kessler, 1985: A surface temperature and moisture parameterization for use in mesoscale numerical models. Preprints, *Seventh Conf. on Numerical Weather Prediction*, Montreal, QC, Canada, Amer. Meteor. Soc., 355–358.

Vijayakumar, G., K. Parameswaran, and R. Rajan, 1998: Aerosols in the atmospheric boundary layer and its association with surface wind speed at a coastal site. *J. Atmos. Sol.-Terr. Phys.*, **60,** 1531–1542.

Xu, L., S. Raman, R. V. Madala, and R. Hodur, 1996: A non-hydrostatic modeling study of surface moisture effects on mesoscale convection induced by sea breeze circulation. *Meteor. Atmos. Phys.*, **58,** 102–122.